

Delay-Phase Precoding for Wideband THz Massive MIMO

Linglong Dai, Jingbo Tan, and H. Vincent Poor

Abstract

Benefiting from tens of GHz bandwidth, terahertz (THz) communication is considered to be a promising technology to provide ultra-high speed data rates for future 6G wireless systems. To compensate for the serious propagation attenuation of THz signals, massive multiple-input multiple-output (MIMO) with hybrid precoding can be utilized to generate directional beams with high array gains. However, the standard hybrid precoding architecture based on frequency-independent phase-shifters cannot cope with the beam split effect in THz massive MIMO systems, where the directional beams will split into different physical directions at different subcarrier frequencies. The beam split effect will result in a serious array gain loss across the entire bandwidth, which has not been well investigated in THz massive MIMO systems. In this paper, we first reveal and quantify the seriousness of the beam split effect in THz massive MIMO systems by analyzing the array gain loss it causes. Then, we propose a new precoding architecture called delay-phase precoding (DPP) to mitigate this effect. Specifically, the proposed DPP introduces a time delay network as a new precoding layer between radio-frequency chains and phase-shifters in the standard hybrid precoding architecture. In this way, conventional phase-controlled analog beamforming can be converted into delay-phase controlled analog beamforming. Unlike *frequency-independent* phase shifts, the time delay network introduced in the DPP can realize *frequency-dependent* phase shifts, which can be designed to generate frequency-dependent beams towards the target physical direction across the entire THz bandwidth. Due to the joint control of delay and phase, the proposed DPP can significantly relieve the array gain loss caused by the beam split effect. Furthermore, we propose a hardware structure by using true-time-delayers to realize frequency-dependent phase shifts for realizing the concept of DPP. Theoretical analysis and simulation results show

A part of this paper was presented in the IEEE Global Communications Conference (GLOBECOM'19) [1].

Linglong Dai and Jingbo Tan are with the Beijing National Research Center for Information Science and Technology (BNRist) as well as the Department of Electronic Engineering, Tsinghua University, Beijing 100084, China (E-mails: daill@tsinghua.edu.cn; tanjb17@mails.tsinghua.edu.cn).

H. Vincent Poor is with the Department of Electrical Engineering, Princeton University, Princeton, NJ 08544, USA (E-mail: poor@princeton.edu).

This work was supported in part by the National Key Research and Development Program of China (Grant No. 2020YFB1807201), in part by the National Natural Science Foundation of China (Grant No. 62031019), and in part by the U.S. National Science Foundation under Grants CCF-0939370 and CCF-1908308.

that the proposed DPP can significantly mitigate the beam split effect across the entire THz bandwidth, and it can achieve near-optimal achievable rate performance with higher energy efficiency than the conventional hybrid precoding architecture.

Index Terms

THz communication, massive MIMO, hybrid precoding, beam split.

I. INTRODUCTION

Because of the tenfold increase in bandwidth it can provide, terahertz (THz) communication is considered to be a promising technology to support the rapid growth of the data traffic in future 6G wireless systems [2]–[7]. Compared with the typical bandwidth of several GHz in the millimeter-wave (mmWave) band (30-100 GHz) for 5G, the THz band (0.1-10 THz) for 6G is capable of providing at least 10 GHz bandwidth or even much larger [6], [8]. However, THz signals suffer from severe propagation attenuation due to the very high carrier frequencies, which is a major obstacle to practical THz communications [2]. Massive multiple-input multiple-output (MIMO), which utilizes a large antenna array to generate directional beams with high array gains, can be used to compensate for such severe signal attenuation in THz communications. Consequently, THz massive MIMO is very promising for future 6G wireless communications [9]–[11]. Similar to mmWave massive MIMO, hybrid precoding has been recently considered for THz massive MIMO to relieve the substantial power consumption of THz radio-frequency (RF) chains [12]. The key idea of hybrid precoding is to decompose the high-dimensional fully-digital precoder into a high-dimensional analog beamformer realized by phase-shifters (PSs) and a low-dimensional digital precoder [13]. Thus, a significantly reduced number of RF chains can be used. Thanks to the sparsity of THz channels [14], a small number of RF chains are still sufficient to fully achieve the multiplexing gain in THz massive MIMO systems [13]–[15].

A. Prior works

In the conventional hybrid precoding architecture, the analog beamformer will generate directional beams aligned with the physical directions of the channel path components to realize the full array gain [15]. Such an analog beamformer works well for narrowband systems. However, for the wideband 5G mmWave massive MIMO systems, the beams at different subcarrier frequencies will point to different physical directions due to the use of the *frequency-independent*

PSs [15], which results in an array gain loss. To deal with the array gain loss incurred by this effect, called beam squint [16], several methods have been proposed for mmWave massive MIMO systems [17]–[20]. Specifically, the hybrid precoding problem in orthogonal frequency division multiplexing (OFDM) based wideband massive MIMO systems was formulated in [17], where a near-optimal closed-form solution was developed. Aiming at improving the performance of hybrid precoding, an alternating optimization algorithm was proposed in [18], which iteratively optimized the analog beamformer and digital precoder to achieve near-optimal achievable rate performance across the entire bandwidth. In addition, codebooks containing beams with wide beamwidths were designed to reduce the array gain loss caused by the beam squint effect in [19], [20]. Specifically, the wide beams were designed in [19] by maximizing the minimum array gain achieved at all subcarriers, while, a semidefinite relaxation method was utilized in [20] to maximize the total array gain across the entire bandwidth achieved by the wide beams. These methods [17]–[20] are effective for improving the achievable rate performance, as the beams only slightly squint and the array gain loss is not serious in wideband mmWave massive MIMO systems.

However, the methods of [17]–[20] are not valid for wideband THz massive MIMO systems. Due to the much wider bandwidth of THz signals and much larger number of antennas to be used, beams at different subcarriers will split into totally separated physical directions. This effect, called *beam split* in this paper, which is a key difference between mmWave and THz massive MIMO systems, brings a new fundamental challenge for THz communications. Specifically, unlike the situation under the beam squint effect where the beams can still cover the user across the entire bandwidth, the beams generated by frequency-independent PSs can only be aligned with the target user over a small portion of all subcarriers around the central frequency due to beam split effect. This indicates that only the beams around the central frequency can achieve high array gain, while the beams at most other subcarriers suffer from a serious array gain loss. Therefore, the beam split effect will result in a severe achievable rate degradation, and counteract the achievable rate gain benefiting from the bandwidth increase in THz massive MIMO systems. To our best knowledge, the beam split effect has not been investigated in THz massive MIMO systems, and there are no existing solutions to this fundamental challenge.

B. Our contributions

In this paper, we first analyze the performance loss caused by the beam split effect, and then we propose the delay-phase precoding (DPP) architecture to mitigate the beam split effect in THz massive MIMO systems. Specifically, the contributions of this paper can be summarized as follows.

- We first reveal and quantify the beam split effect, i.e., the THz rainbow, in wideband THz massive MIMO systems. Specifically, the relationship between the array gain loss and the system parameters, including the bandwidth, the central carrier frequency, path directions, and the number of antennas, is analyzed. Based on this analysis, we define a metric called the beam split ratio to evaluate the degree of the beam split effect, which clearly shows how serious the beam split effect is in wideband THz massive MIMO systems.
- We propose a new precoding architecture, namely DPP, to mitigate the beam split effect. In the proposed DPP, a new precoding layer, which is a time delay (TD) network, is introduced between the RF chains and frequency-independent PSs in the conventional hybrid precoding architecture. The PSs are still used to generate beams aligned with the target physical direction, while the time delays in the TD network are designed to make the beams aligned with the target physical directions across the entire bandwidth. In this way, the DPP architecture can convert *frequency-independent* phase controlled beamforming into *frequency-dependent* delay-phase controlled beamforming, which can significantly alleviate the array gain loss caused by the beam split effect.
- We further prove that beams generated by the DPP architecture are aligned with the target physical direction at different subcarriers, and they can achieve near-optimal array gain across the entire bandwidth.
- Finally, a hardware structure called true-time-delayers based DPP (TTD-DPP) is proposed to realize the concept of DPP, where the TD network is realized by a small number of TTDs between the RF chains and the PS network. The analysis illustrates that the proposed TTD-DPP structure is able to achieve a near-optimal achievable rate, which is supported by extensive simulation results.

C. Organization and notation

Organization: The remainder of the paper is organized as follows. In Section II, a system model of wideband THz massive MIMO with the conventional hybrid precoding architecture

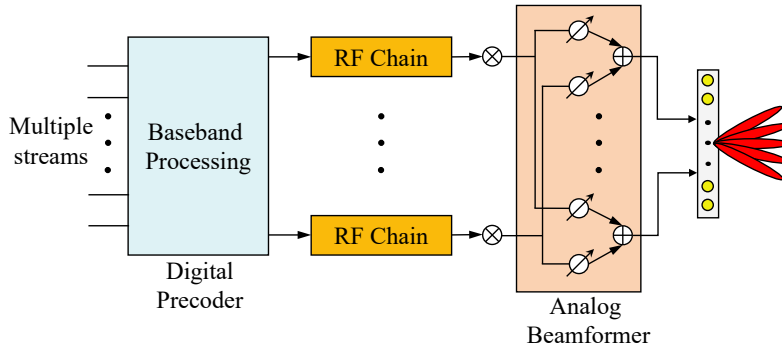


Fig. 1. The classical hybrid precoding architecture [15].

is provided. In Section III, we analyze the array gain loss caused by the beam split effect, and propose the DPP architecture, together with the array gain performance analysis. Then, a hardware structure based on true-time-delays is proposed to realize the concept of DPP in Section IV. In Section V, the simulation results are provided. Finally, conclusions are drawn in Section VI.

Notation: Lower-case and upper-case boldface letters represent vectors and matrices, respectively; $(\cdot)^T$, $(\cdot)^H$, $\|\cdot\|_F$, and $\|\cdot\|_k$ denote the transpose, conjugate transpose, Frobenius norm, and k -norm of a matrix, respectively; $\mathbf{H}_{[i,j]}$ denotes the element of matrix \mathbf{H} at the i -th row and the j -th column; $\mathbb{E}(\cdot)$ denotes the expectation; $|\cdot|$ denotes the absolute value; \mathbf{I}_N represents the identity matrix of size $N \times N$; $\text{blkdiag}(\mathbf{A})$ denotes a block diagonal matrix where each column of \mathbf{A} represents the diagonal blocks of the matrix $\text{blkdiag}(\mathbf{A})$; $\mathcal{CN}(\mu, \Sigma)$ denotes the Gaussian distribution with mean μ and covariance Σ ; and finally, $\mathcal{U}(a, b)$ represents the uniform distribution between a and b .

II. SYSTEM MODEL OF THZ MASSIVE MIMO

We first consider a THz massive MIMO system with the conventional hybrid precoding as shown in Fig. 1. The base station (BS) employs N_{RF} RF chains and an N_t -antenna uniform linear array (ULA)¹. An N_r -antenna user is served and N_s data streams are transmitted simultaneously by the BS (usually we have $N_s = N_r \leq N_{\text{RF}} \ll N_t$). To realize wideband transmission, the widely used orthogonal frequency division multiplexing (OFDM) with M subcarriers is

¹In this paper, we consider the ULA for simplicity, but the analysis of the beam split effect and the correspondingly proposed DPP architecture can be easily extended to the uniform planar array (UPA) [21], which has similar channel form as ULA.

considered. The downlink received signal $\mathbf{y}_m \in \mathcal{C}^{N_r \times 1}$ at the m -th subcarrier ($m = 1, 2, \dots, M$) can be expressed as [15]

$$\mathbf{y}_m = \sqrt{\rho} \mathbf{H}_m^H \mathbf{A} \mathbf{D}_m \mathbf{s}_m + \mathbf{n}_m, \quad (1)$$

where $\mathbf{H}_m \in \mathcal{C}^{N_t \times N_r}$ denotes the frequency-domain channel at the m -th subcarrier, $\mathbf{A} \in \mathcal{C}^{N_t \times N_{RF}}$, with constraint $|\mathbf{A}_{[i,j]}| = \frac{1}{\sqrt{N_t}}$ due to the use of frequency-independent PSs [22], is the frequency-independent analog beamformer identical over all M subcarriers, $\mathbf{D}_m \in \mathcal{C}^{N_{RF} \times N_s}$ is the frequency-dependent digital precoder at the m -th subcarrier satisfying the transmission power constraint $\|\mathbf{A} \mathbf{D}_m\|_F^2 = N_s$, $\mathbf{s}_m \in \mathcal{C}^{N_s \times 1}$ represents the transmitted signal at the m -th subcarrier with the normalized power $\mathbb{E}(\mathbf{s}_m \mathbf{s}_m^H) = \frac{1}{N_s} \mathbf{I}_{N_s}$, ρ is the average received power, and $\mathbf{n}_m \in \mathcal{C}^{N_s \times 1}$ denotes the additive white Gaussian noise (AWGN) at the m -th subcarrier following the Gaussian distribution $\mathcal{CN}(0, \sigma^2 \mathbf{I}_{N_s})$ with σ^2 being the noise power.

In this paper, we consider the widely used wideband ray-based channel model [9] for THz communications. We denote f_c as the central frequency and B as the bandwidth. Then, the time-domain channel h_{n_t, n_r} between the n_t -th antenna of the BS and the n_r antenna of the user with $n_t \in 1, 2, \dots, N_t$ and $n_r \in 1, 2, \dots, N_r$ can be denoted as

$$h_{n_t, n_r} = \sum_{l=1}^L g_l \delta(t - \tau_l - (n_t - 1) \frac{d}{c} \sin \tilde{\theta}_l - (n_r - 1) \frac{d}{c} \sin \tilde{\phi}_l), \quad (2)$$

where L denotes the number of resolvable paths, g_l and τ_l represent the path gain and path delay of the l -th path, $\tilde{\theta}_l, \tilde{\phi}_l \in [-\pi/2, \pi/2]$ are the frequency-independent physical directions of the l -th path at the BS side and the user side respectively, d is the antenna spacing usually set according to the central frequency f_c as $d = \frac{\lambda}{2} = \frac{c}{2f_c}$ with λ denoting the wavelength at the central frequency f_c and cannot be changed after the antenna array has been fabricated, and c denotes the light speed in the free space. In (2), $(n_t - 1) \frac{d}{c} \sin \tilde{\theta}_l$ and $(n_r - 1) \frac{d}{c} \sin \tilde{\phi}_l$ denote the time delays caused by the physical directions of the l -th path at the n_t -th antenna of the BS and that at the n_r -th antenna of the user, respectively.

For the m -th subcarrier with the frequency $f_m = f_c + \frac{B}{M}(m - 1 - \frac{M-1}{2})$, the frequency-domain channel \mathbf{H}_m can be presented by the discrete Fourier transform (DFT) of the time-domain channel in (2) as

$$\mathbf{H}_m = \sum_{l=1}^L g_l e^{-j2\pi\tau_l f_m} \mathbf{f}_t(\tilde{\theta}_{l,m}) \mathbf{f}_r(\tilde{\phi}_{l,m})^H, \quad (3)$$

where $\mathbf{f}_t(\tilde{\theta}_{l,m})$ and $\mathbf{f}_r(\tilde{\phi}_{l,m})$ are the array responses at the BS side and the user side, and they

can be presented by setting $d = \frac{c}{2f_c}$ as

$$\begin{aligned}\mathbf{f}_t(\bar{\theta}_{l,m}) &= \frac{1}{\sqrt{N_t}} \left[1, e^{j\pi\bar{\theta}_{l,m}}, e^{j\pi 2\bar{\theta}_{l,m}}, \dots, e^{j\pi(N_t-1)\bar{\theta}_{l,m}} \right]^H, \\ \mathbf{f}_r(\bar{\phi}_{l,m}) &= \frac{1}{\sqrt{N_r}} \left[1, e^{j\pi\bar{\phi}_{l,m}}, e^{j\pi 2\bar{\phi}_{l,m}}, \dots, e^{j\pi(N_r-1)\bar{\phi}_{l,m}} \right]^H,\end{aligned}\quad (4)$$

where $\bar{\theta}_{l,m}$ and $\bar{\phi}_{l,m} \in [-1, 1]$ denote the spatial directions at the BS side and the user side of the l -th path component at the m -th subcarrier, respectively. The spatial directions are the directions of the channel path components in the spatial domain. Since (3) is obtained by the DFT of (2), we can obtain the relationship between the spatial directions $(\theta_{l,m}, \phi_{l,m})$ in (3) and the physical directions $(\tilde{\theta}_l, \tilde{\phi}_l)$ in (2) as follows

$$\begin{aligned}\bar{\theta}_{l,m} &= 2d \frac{f_m}{c} \sin \tilde{\theta}_l, \\ \bar{\phi}_{l,m} &= 2d \frac{f_m}{c} \sin \tilde{\phi}_l.\end{aligned}\quad (5)$$

For simplification, in this paper, we use $\theta_l = \sin \tilde{\theta}_l$ and $\phi_l = \sin \tilde{\phi}_l$ to denote the physical directions, where $\theta_l, \phi_l \in [-1, 1]$.

By considering the channel model (3)-(5), we will introduce the beamforming mechanism in the next section, based on which the beam split effect in THz massive MIMO will be revealed and the DPP architecture will be proposed.

III. DELAY-PHASE PRECODING FOR THZ MASSIVE MIMO

In this section, we will first introduce the beamforming mechanism in massive MIMO systems. Based on the beamforming mechanism, the beam split effect in THz massive MIMO will be revealed by analyzing the severe array gain loss caused by it. Then, to mitigate the severe array gain loss in THz massive MIMO systems, the DPP architecture will be proposed, and the corresponding array gain performance analysis will also be provided.

A. Beamforming mechanism

Generally, in THz massive MIMO systems with the hybrid precoding architecture, the analog beamformer is designed to generate beams towards the physical directions of the channel path components, to compensate for the severe path loss [15], while, the digital precoder is designed based on the determined analog beamformer to realize the spatial multiplexing gain. Therefore, whether the beams generated by the beamformer can precisely point to the physical directions of

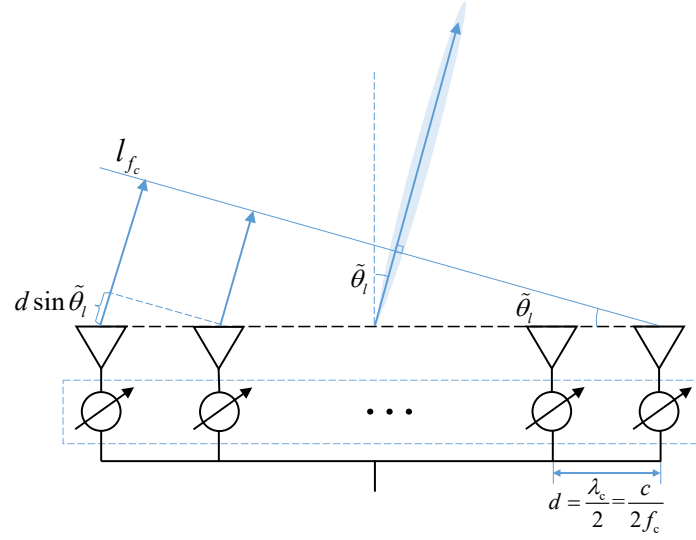


Fig. 2. Beamforming mechanism.

channel path components has a crucial impact on the achievable rate performance. Here, taking the narrowband THz massive MIMO system as an example, we will introduce the beamforming mechanism.

Without loss of generality, we consider the l -th path component with the physical direction θ_l of the channel in (3). Usually, the l -th column of the analog beamformer \mathbf{A} in (1), i.e., the analog beamforming vector $\mathbf{a}_l = \mathbf{A}_{[:,l]}$, is used to generate a directional beam towards the l -th path's physical direction θ_l , which has been proved to be near-optimal [15]. Specifically, the beamforming mechanism is to make electromagnetic waves that transmitted by different antenna elements form an equiphase surface, which is perpendicular to the target physical direction θ_l , as shown in Fig. 2. To achieve this goal, different phase shifts provided by PSs should be compensated at different antenna elements. For instance, the distance difference between adjacent antenna elements reaching the equiphase surface is $d \sin \tilde{\theta}_l = d\theta_l$. Therefore, for narrowband systems where $f_m \approx f_c$, the phase difference that should be compensated between adjacent antenna elements is $-2\pi \frac{d}{\lambda_c} \theta_l = -2\pi \frac{d}{c} f_c \theta_l$, where λ_c denotes the wavelength at the central frequency f_c . As a result, the analog beamforming vector \mathbf{a}_l should be

$$\mathbf{a}_l = \frac{1}{N_t} \left[1, e^{-j2\pi \frac{d}{c} f_c \theta_l}, e^{-j2\pi 2 \frac{d}{c} f_c \theta_l}, \dots, e^{-j2\pi (N_t-1) \frac{d}{c} f_c \theta_l} \right]^T = \mathbf{f}_t \left(2 \frac{d}{c} f_c \theta_l \right) = \mathbf{f}_t(\theta_l). \quad (6)$$

Based on the analog beamforming vector designed in (6), the normalized array gain $\eta(\mathbf{a}_l, \theta_l, f_c)$

achieved by \mathbf{a}_l in the physical direction θ_l at the central frequency f_c is

$$\eta(\mathbf{a}_l, \theta_l, f_c) = \left| \mathbf{f}_t(2d\frac{f_c}{c}\theta_l)^H \mathbf{a}_l \right| \stackrel{(a)}{=} |\mathbf{f}_t(\theta_l)^H \mathbf{a}_l| \approx |\mathbf{f}_t(\theta_l)^H \mathbf{f}_t(\theta_l)| = 1, \quad (7)$$

where (a) comes from $d = \frac{\lambda_c}{2} = \frac{c}{2f_c}$. It is clear from (7) that by setting the analog beamforming vector $\mathbf{a}_l = \mathbf{f}_t(\theta_l)$, the optimal normalized array gain of 1 can be achieved at the central frequency f_c . Thus, considering $f_m \approx f_c, m = 1, 2, \dots, M$, the narrowband systems can enjoy the satisfying normalized array gain across the entire bandwidth B .

B. Beam split effect

In wideband systems, since the PSs are *frequency-independent* and the antenna spacing d is set according to the central frequency f_c , the analog beamforming vector \mathbf{a}_l is usually set the same as (6), which is also *frequency-independent*. However, considering the frequency-independent phase shifts will cause frequency-dependent time delays, i.e., phase shift $\Delta\theta$ corresponds to time delay $-2\pi f_m \Delta\theta$ at subcarrier frequency f_m , the equiphase surfaces generated by the frequency-independent analog beamforming vector \mathbf{a}_l will be separated at different subcarriers. Therefore, the beams generated by the frequency-independent analog beamforming vector \mathbf{a}_l will point to different physical directions surrounding the target physical direction θ_l at different subcarriers. This effect is called beam squint in mmWave massive MIMO systems [16]. Fortunately, since the beams at different subcarriers can still cover the user by their mainlobes, the array gain degradation caused by the beam squint is small in mmWave massive MIMO systems and can be solved by several existing methods [17]–[20].

However, the beam squint effect will be severely aggregated in THz massive MIMO systems for two reasons. Firstly, due to the much larger bandwidth of THz massive MIMO systems, the physical direction deviations between the physical directions that the beams at different subcarriers are aligned with and the target physical direction will significantly increase. Secondly, the much larger number of antennas in THz massive MIMO systems leads to an extremely narrow beamwidth. Due to the above two reasons, the beams at different subcarrier frequencies may be totally split into separated physical directions in THz massive MIMO systems as shown in Fig. 3 (a). Thus, unlike the beam squint effect, an unacceptable array gain loss occurs since most of the beams at different subcarriers cannot cover the user in their mainlobes. Unfortunately, this aggregated effect cannot be solved by the existing methods based on the classical hybrid precoding architecture [17]–[20], and it has not been well addressed in the literature. To this

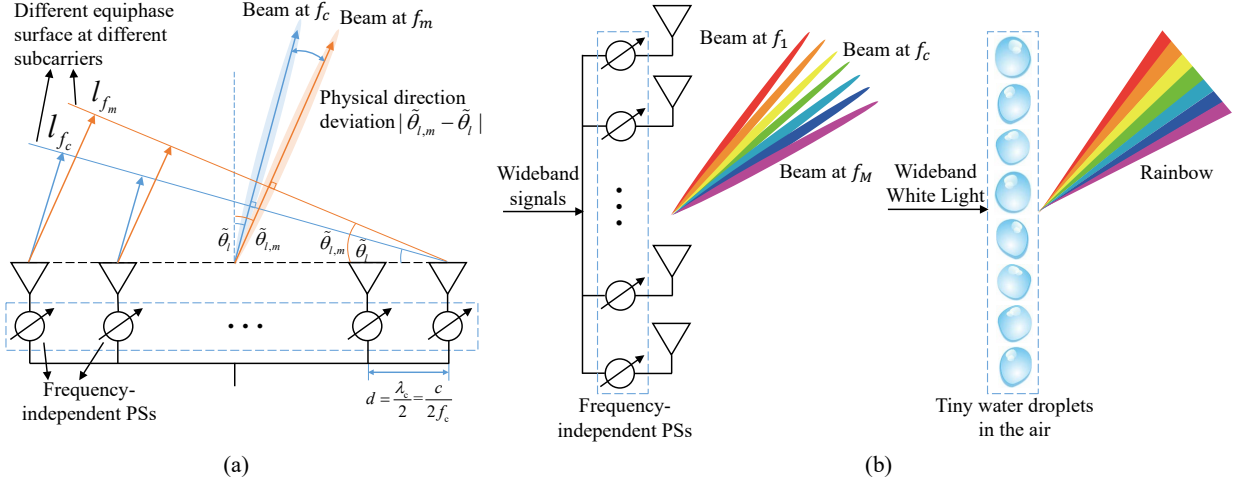


Fig. 3. The mechanism of the beam split effect: (a) The beam split at subcarrier frequency f_m . $\tilde{\theta}_{l,m}$ denotes the physical direction that the beam at subcarrier frequency f_m is aligned with; (b) The analogy between the beam split effect and the rainbow over the large bandwidth. f_1 and f_M denote the lowest subcarrier frequency and the highest subcarrier frequency, respectively.

end, we define the effect that the beams at different subcarriers are totally separated as the **beam split effect**. A simple analogy between the beam split effect and the rainbow can illustrate the mechanism of the beam split effect. As shown in Fig. 3 (b), because the tiny water droplets in the air have different refractive indices for the wideband white light composed of different frequencies, the pure light of different frequencies will totally separate and eventually produce the rainbow. Just like the rainbow, frequency-independent PSs cause different “refractive indices” for THz signals at different frequencies, and thus leads to totally separated beams at different frequencies. Therefore, we can also call the beam split effect as “**THz rainbow**”.

The beam split effect will result in an unacceptable array gain loss, which is mainly determined by the bandwidth and the number of antennas. Specifically, the following **Lemma 1** will theoretically quantify the relationship between the array gain loss caused by the beam split effect and the system parameters such as bandwidth and the number of antennas. Notice that we utilize $\theta_{l,m} = \sin \tilde{\theta}_{l,m} \in [-1, 1]$ denotes the physical direction that the beam at subcarrier frequency f_m is aligned with for simplifying the expression.

Lemma 1. *The beam generated by the analog beamforming vector $\mathbf{a}_l = \mathbf{f}_t(\theta_l)$ is aligned with the physical direction $\theta_{l,m}$ satisfying $\theta_{l,m} = \frac{\theta_l}{\xi_m}$, where $\xi_m = \frac{f_m}{f_c}$ is the normalized frequency. Furthermore, when $|(\xi_m - 1)\theta_l| \geq \frac{2}{N_t}$, the normalized array gain $\eta(\mathbf{a}_l, \theta_l, f_m)$ achieved by the*

analog beamforming vector \mathbf{a}_l in the physical direction θ_l at subcarrier frequency f_m satisfies

$$\eta(\mathbf{a}_l, \theta_l, f_m) \leq \frac{1}{N_t \sin \frac{3\pi}{2N_t}}. \quad (8)$$

Proof: The normalized array gain achieved by the analog beamforming vector \mathbf{a}_l in an arbitrary physical direction $\theta \in [-1, 1]$ at subcarrier frequency f_m can be denoted as $\eta(\mathbf{a}_l, \theta, f_m) = \left| \mathbf{f}_t(2d\frac{f_m}{c}\theta)^H \mathbf{a}_l \right|$. Then, we have

$$\begin{aligned} \eta(\mathbf{a}_l, \theta, f_m) &\stackrel{(a)}{=} \left| \mathbf{f}_t(2d\frac{f_m}{c}\theta)^H \mathbf{f}_t(\theta_l) \right| \stackrel{(b)}{=} \frac{1}{N_t} \left| \sum_{n=0}^{N_t-1} e^{jn\pi(\xi_m\theta - \theta_l)} \right| \\ &\stackrel{(c)}{=} \left| \frac{\sin \frac{N_t\pi}{2}(\xi_m\theta - \theta_l)}{N_t \sin \frac{\pi}{2}(\xi_m\theta - \theta_l)} e^{-j\frac{(N_t-1)\pi}{2}(\xi_m\theta - \theta_l)} \right|, \end{aligned} \quad (9)$$

where (a), (b), and (c) come from $\mathbf{a}_l = \mathbf{f}_t(\theta_l)$, (4), and the equation $\sum_{n=0}^{N_t-1} e^{jn\pi\alpha} = \frac{\sin \frac{N_t\pi}{2}\alpha}{N_t \sin \frac{\pi}{2}\alpha} e^{-j\frac{(N_t-1)\pi}{2}\alpha}$, respectively. Therefore, the array gain achieved by the analog beamforming vector \mathbf{a}_l in an arbitrary physical direction θ at subcarrier frequency f_m can be denoted as

$$\eta(\mathbf{a}_l, \theta, f_m) = \frac{1}{N_t} |\Xi_{N_t}((\xi_m\theta - \theta_l))|, \quad (10)$$

where $\Xi_{N_t}(x) = (\sin \frac{N_t\pi}{2}x) / (\sin \frac{\pi}{2}x)$ is the Dirichlet sinc function [23]. It is known that the Dirichlet sinc function has the power-focusing property, where the maximum is $|\Xi_{N_t}(0)| = N_t$ and the value of $|\Xi_{N_t}(x)|$ decreases sharply as $|x|$ increases [23].

Denote $\theta_{l,m}$ as the physical direction that the analog beamforming vector \mathbf{a}_l is aligned with at subcarrier frequency f_m . The analog beamforming vector \mathbf{a}_l should achieve the largest array gain in the physical direction $\theta_{l,m}$ as $\theta_{l,m} = \arg \max_{\theta} \eta(\mathbf{a}_l, \theta, f_m)$. Therefore, considering the property of Dirichlet sinc function that the maximum is $|\Xi_{N_t}(0)| = N_t$, the physical direction $\theta_{l,m}$ should satisfy $\xi_m\theta_{l,m} - \theta_l = 0$ according to (10). Hence, we can obtain the physical direction $\theta_{l,m}$ that the analog beamforming vector \mathbf{a}_l is aligned with at subcarrier frequency f_m should satisfy

$$\theta_{l,m} = \frac{\theta_l}{\xi_m}. \quad (11)$$

Moreover, by substituting $\theta = \theta_l$ into (10), the normalized array gain $\eta(\mathbf{a}_l, \theta_l, f_m)$ achieved by the analog beamforming vector \mathbf{a}_l in the physical direction θ_l at subcarrier frequency f_m can be denoted as $\eta(\mathbf{a}_l, \theta_l, f_m) = \frac{1}{N_t} |\Xi_{N_t}((\xi_m - 1)\theta_l)|$. According to the power-focusing property of the Dirichlet sinc function, when $|(\xi_m - 1)\theta_l| \geq \frac{2}{N_t}$, $|(\xi_m - 1)\theta_l|$ locates out of the mainlobe of the

Dirichlet sinc function $|\Xi_{N_t}(x)|$, which means the beam generated by the analog beamforming vector \mathbf{a}_l cannot cover the user with its mainlobe at the subcarrier frequency f_m , and a severe array gain loss will occur. Specifically, considering that the maximum value of $|\Xi_{N_t}(x)|$ when $|x| \geq \frac{2}{N_t}$ is $(1/N_t) \sin \frac{3\pi}{2N_t}$, we have

$$|\eta(\mathbf{a}_l, \theta_l, f_m)| = \frac{1}{N_t} |\Xi_{N_t}((\xi_m - 1)\theta_l)| \leq \frac{1}{N_t \sin \frac{3\pi}{2N_t}}, \quad (12)$$

when $|(\xi_m - 1)\theta_l| \geq \frac{2}{N_t}$, which means the beam generated by the analog beamforming vector \mathbf{a}_l cannot cover the user with its mainlobe at the subcarrier frequency f_m . ■

Lemma 1 has revealed two major parameters that affect the array gain loss caused by the beam split effect, i.e., the bandwidth B and the number of antennas N_t . Specifically, when the bandwidth B and the number of antennas N_t are large, the condition $|(\xi_m - 1)\theta_l| \geq \frac{2}{N_t}$ can be easily satisfied at most of subcarriers, which indicates that beams at most of subcarriers cannot cover the user with their mainlobes. As a result, the achieved array gains at most of the subcarriers are upper bounded by $\frac{1}{N_t \sin \frac{3\pi}{2N_t}}$ as shown in (12), which are extremely small with a large number of antennas N_t . This implies that the severe array gain loss will occur at most of subcarriers due to the beam split effect. The array gain loss caused by the beam split effect can be explained from the physical perspective. Firstly, according to (11), the physical direction $\theta_{l,m}$ that the beam generated by the analog beamforming vector \mathbf{a}_l is aligned with, is determined by the subcarrier frequency f_m due to $\xi_m = f_m/f_c$. Hence, when the bandwidth B becomes larger, the physical direction deviation, i.e., the interval $|\theta_{l,m} - \theta_l|$ between the target physical direction θ_l and the actual physical direction $\theta_{l,m}$, increases with the subcarrier index m . Secondly, a larger number of antennas N_t will result in a narrower beamwidth as $\frac{4}{N_t}$. Consequently, considering the large bandwidth B and the large number of antennas N_t in THz massive MIMO systems, there will be a large physical direction deviation and an extremely narrow beamwidth at most of the subcarrier frequencies. Under this circumstances, the beams at different subcarriers will become totally separated, which means the beam split effect as shown in Fig. 3 occurs. Due to the beam split effect, the beams at different subcarriers cannot cover the user with their mainlobes, which will induce a severe array gain loss.

From **Lemma 1**, we know that the array gain loss caused by the beam split effect is not only determined by the bandwidth B , but also related to the number of antennas N_t . Hence, it is important to define a single metric to evaluate the degree of the beam split effect. Actually,

from the description above, we can conclude that the degree of the beam split effect or the array gain loss caused by the beam split effect, is determined by the “relatively offset” between the physical direction deviation and the beamwidth. When the relatively offset is large, beams tend to split at different subcarriers, and cannot cover the user with their mainlobes, which finally results in a severe array gain loss. Following this idea, we can define a metric called beam split ratio (BSR) to evaluate the degree of the beam split effect. Specifically, the BSR is defined as the expectation of the ratio between the physical direction deviation and half of the beamwidths for all subcarrier frequencies and physical directions as

$$\text{BSR} = \frac{1}{2M} \int_{-1}^1 \sum_{m=1}^M \frac{|\theta_{l,m} - \theta_l|}{2/N_t} d\theta_l = \int_{-1}^1 \frac{1}{M} \sum_{m=1}^M \frac{1}{2} |N_t(\xi_m - 1)\theta_l| d\theta_l, \quad (13)$$

where $|\theta_{l,m} - \theta_l|$ is the physical direction deviation, and $2/N_t$ denotes half of the beamwidth. Note that the condition $|(\xi_m - 1)\theta_l| \geq \frac{2}{N_t}$ or $\frac{1}{2}|N_t(\xi_m - 1)\theta_l| \geq 1$ means the beam at the subcarrier frequency f_m cannot cover the user with its mainlobe, and the BSR is defined as the average of $\frac{1}{2}|N_t(\xi_m - 1)\theta_l|$ in (13). Therefore, we can suppose that if $\text{BSR} > 1$, the beams at different subcarriers cannot cover the user with their mainlobes on average and the beam split effect occurs. On the contrary, when $\text{BSR} < 1$, the beams will slightly squint and only the beam squint effect occurs. By using the proposed metric BSR, we can simply evaluate the degree of the beam split effect. A larger BSR means a stronger degree of the beam split effect and a more serious array gain loss. For instance, for a THz massive MIMO system with parameters $f_c = 300$ GHz, $N_t = 256$, $M = 128$ and $B = 30$ GHz, $\text{BSR} = 1.6 > 1$, which indicates the beam split effect really happens in THz massive MIMO systems. While, for a mmWave massive MIMO, the BSR is usually smaller than 1, e.g., $\text{BSR} = 0.29$ for a mmWave massive MIMO system with parameters $f_c = 28$ GHz, $N_t = 64$, $M = 128$ and $B = 2$ GHz. This indicates that the beam squint rather than the beam split happens in mmWave massive MIMO. Considering that the performance loss caused by the beam squint is limited compared with the performance loss caused by the beam split, we can conclude that the beam split effect is one of the key differences between mmWave and THz massive MIMO systems.

To better illustrate the beam split effect, we provide the normalized array gain comparison achieved by the analog beamforming vector \mathbf{a}_l between sub-6G MIMO system, mmWave massive MIMO system, and THz massive MIMO system in Fig. 4. The BSRs of them are 0.03, 0.29, and 1.6, respectively. We can observe from Fig. 4 that in sub-6G and mmWave systems with

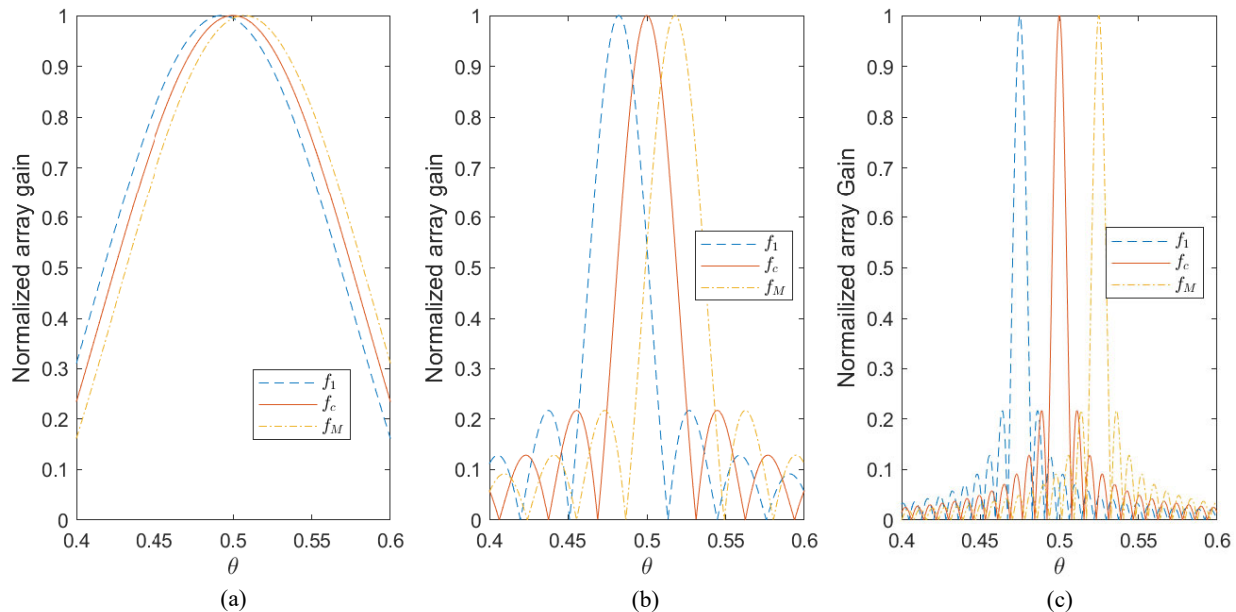


Fig. 4. Normalized array gain achieved by the classical hybrid precoding architecture with analog beamforming vector $\mathbf{a}_l = \mathbf{f}_l(\theta_l)$ with respect to the physical direction θ , where f_1 and f_M denote the lowest subcarrier frequency and the highest subcarrier frequency: (a) Sub-6GHz MIMO system with $\theta_l = 0.5$, $f_c = 3.5$ GHz, $B = 0.1$ GHz, $N_t = 16$ and $M = 128$; (b) MmWave massive MIMO system with $\theta_l = 0.5$, $f_c = 28$ GHz, $B = 2$ GHz, $N_t = 64$ and $M = 128$; (c) THz massive MIMO system with $\theta_l = 0.5$, $f_c = 300$ GHz, $B = 30$ GHz, $N_t = 256$ and $M = 128$.

$\text{BSR} < 1$, the beams at subcarrier frequencies f_1 and f_M slightly squint from the beam at the central frequency f_c . The array gain loss across the entire bandwidth is limited. Nevertheless, for THz massive MIMO systems, the beams at subcarrier frequencies f_1 and f_M are totally separated from the beam at the central frequency f_c , and point to the physical direction far away from θ_l . This beam split effect will cause serious array gain loss across the entire bandwidth. To better reveal the array gain loss caused by the beam split effect, Fig. 5 illustrates the normalized array gain achieved by the analog beamforming vector \mathbf{a}_l at different subcarriers m for sub-6G MIMO system, mmWave MIMO system, and THz massive MIMO system. The system parameters are the same as these in Fig. 4. We can see from Fig. 5 that the analog beamforming vector \mathbf{a}_l suffers from a severe array gain loss in wideband THz massive MIMO system, while, the array gain losses in sub-6G and mmWave systems are not serious. These results are consistent with the BSRs of these systems as $0.03 < 0.29 < 1 < 1.6$, which indicates the beam split effect occurs in THz system but not in sub-6G or mmWave system. Particularly, for more than 50% of subcarriers, e.g., the subcarriers $m \leq 47$ or $m \geq 81$ in THz massive MIMO system, the user will suffer from more than 80% array gain loss.

Such a serious array gain loss incurred by the beam split effect is not acceptable for THz

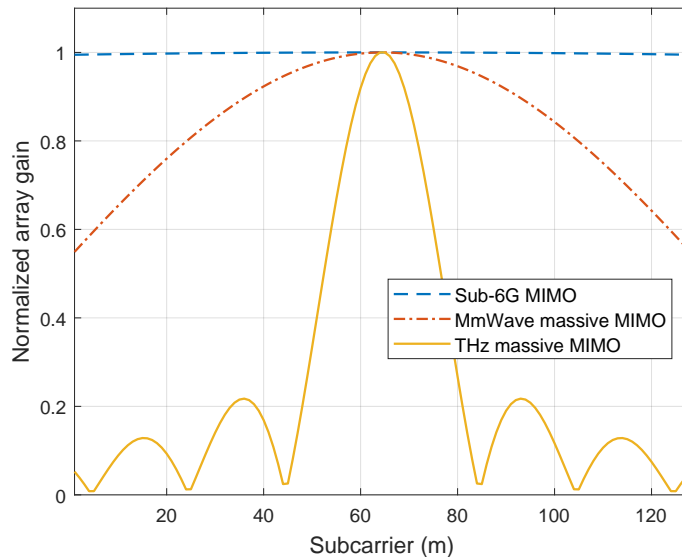


Fig. 5. Normalized array gain achieved by the classical hybrid precoding architecture with analog beamforming vector $\mathbf{a}_l = \mathbf{f}_l(\theta_l)$ in different systems. The system parameters are the same as these in Fig. 4.

communications. However, the existing hybrid precoding methods with frequency-independent PSs cannot solve this problem. In ultrawideband radar systems, the array gain loss incurred by the beam split effect can be solved by utilizing a TTD for each antenna element [24], but this solution is unpractical for hybrid precoding, since a large number of TTDs may bring the unacceptable power consumption and high hardware cost [16]. To our best knowledge, there are no practical solutions to solve the beam split effect in THz massive MIMO systems. To fill in this gap, in the next section we will propose a new precoding architecture called DPP for THz massive MIMO systems.

C. Delay-phase precoding (DPP)

As discussed in Subsection III-B above, due to the beam split effect, the *frequency-independent* beamformer generated by the frequency-independent PSs in the classical hybrid precoding architecture, will result in the severe array gain loss. In this subsection, we will propose a new precoding architecture called DPP to solve this problem. As shown in Fig. 6, compared with the classical hybrid precoding architecture, a TD network is introduced as a new precoding layer between the RF chains and the frequency-independent PS network in the proposed DPP.

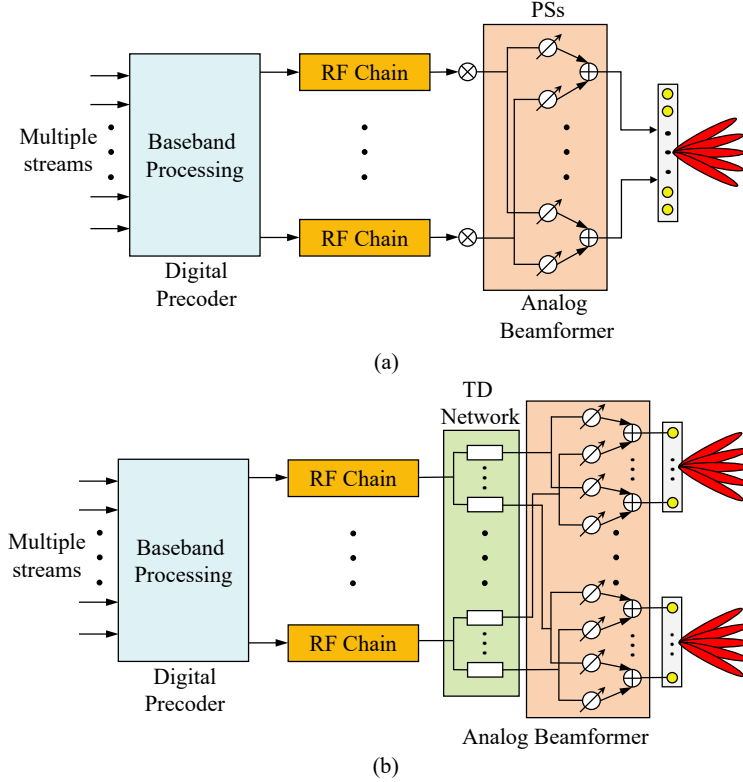


Fig. 6. Precoding architecture comparison: (a) The classical hybrid precoding architecture for mmWave massive MIMO; (b) The proposed DPP architecture for THz massive MIMO.

Specifically, each RF chain is connected to a TD network with K TD elements², and then each TD element is connected to $P = \frac{N_t}{K}$ PSs in a sub-connected manner, similar to the sub-connected hybrid precoding architecture [25]. Therefore, each RF chain still connects to every antenna element through the PSs. The TD network can realize frequency-dependent phase shifts through time delays, e.g., the phase shift $-2\pi f_m t$ can be achieved by the time delay t at the subcarrier frequency f_m . Thus, by utilizing the TD network, the proposed DPP converts the traditional phase-controlled beamformer into delay-phase jointly controlled beamformer, which can realize the *frequency-dependent* beamforming.

Without loss of generality, we consider the l -th channel path component. Since the TD network can provide the frequency-dependent phase shifts, we now utilize the frequency-dependent $\mathbf{a}_{l,m}$ instead of the frequency-independent \mathbf{a}_l to represent the analog beamforming vector generated by the DPP for the l -th path component at the m -th subcarrier. Specifically, the frequency-dependent

² K is a variable parameter in the proposed DPP architecture, which should satisfy that $P = N_t/K$ is an integer. The design principle of K will be discussed later.

analog beamforming vector $\mathbf{a}_{l,m}$ can be denoted as

$$\mathbf{a}_{l,m} = \text{blkdiag}([\bar{\mathbf{a}}_{l,1}, \bar{\mathbf{a}}_{l,2}, \dots, \bar{\mathbf{a}}_{l,K}])\mathbf{p}_{l,m}, \quad (14)$$

where $\bar{\mathbf{a}}_{l,k} \in \mathcal{C}^{P \times 1}$ with $k = 1, 2, \dots, K$ denotes the analog beamforming vector realized by PSs connected to the k -th TD element, so we have $|\bar{\mathbf{a}}_{l,k,[j]}| = \frac{1}{\sqrt{N_t}}$ as usual due to the constraint of constant modulus, and $\mathbf{p}_{l,m} \in \mathcal{C}^{K \times 1}$ composes of the frequency-dependent phase shift realized by K TD elements. Specifically, the k -th element $\mathbf{p}_{l,m,[k]}$ in $\mathbf{p}_{l,m}$ with $k = 1, 2, \dots, K$ satisfies the form $\mathbf{p}_{l,m,[k]} = e^{-j2\pi f_m t_{l,k}}$, where the time delay provided by the k -th TD element is $t_{l,k}$.

Aiming to compensate for the severe array gain loss caused by the beam split effect, the analog beamforming vector $\mathbf{a}_{l,m}$ should generate beams aligned with the target physical direction θ_l at all M subcarriers. In this way, the user can be covered by the beams across the entire bandwidth, and the near-optimal array gain can be achieved. To realize this design goal, we will firstly use the frequency-independent PSs to generate a beam aligned with the target physical direction θ_l as

$$[\bar{\mathbf{a}}_{l,1}^T, \bar{\mathbf{a}}_{l,2}^T, \dots, \bar{\mathbf{a}}_{l,K}^T]^T = \mathbf{f}_t(\theta_l). \quad (15)$$

Then, we utilize the frequency-dependent $\mathbf{p}_{l,m}$ in (14) to rotate the physical direction that the beam $[\bar{\mathbf{a}}_{l,1}^T, \bar{\mathbf{a}}_{l,2}^T, \dots, \bar{\mathbf{a}}_{l,K}^T]^T = \mathbf{f}_t(\theta_l)$ is aligned with from $\theta_{l,m}$ to θ_l . To maintain the directivity of the frequency-dependent beam generated by the analog beamforming vector $\mathbf{a}_{l,m}$, we set $\mathbf{p}_{l,m}$ share the same form as the array response in (4). Specifically, by making the frequency-dependent phase shift $-2f_m t_{l,k} = -(k-1)\beta_{l,m}$ with $k = 1, 2, \dots, K$, $\mathbf{p}_{l,m}$ satisfies

$$\mathbf{p}_{l,m} = [1, e^{-j\pi\beta_{l,m}}, e^{-j2\pi\beta_{l,m}}, \dots, e^{-j\pi(K-1)\beta_{l,m}}]^T, \quad (16)$$

where we define $\beta_{l,m}$ as the direction rotation factor at the m -th subcarrier for the l -th path component. Without loss of generality, we set the value range of the direction rotation factor as $\beta_{l,m} \in [-1, 1]$, due to the periodicity of the $\mathbf{p}_{l,m}$ in (16) with respect to the direction rotation factor $\beta_{l,m}$. By adjusting the direction rotation factor $\beta_{l,m}$, the beam generated by the analog beamforming vector $\mathbf{a}_{l,m}$ can be made to be aligned with the target physical direction θ_l at all M subcarriers. The following **Lemma 2** provides the specific design principle of the direction rotation factor $\beta_{l,m}$, where $\beta_{l,m}$ is determined based on the physical direction θ_l and the subcarrier frequency f_m .

Lemma 2. When $\bar{\mathbf{a}}_{l,k}$ satisfies $[\bar{\mathbf{a}}_{l,1}^T, \bar{\mathbf{a}}_{l,2}^T, \dots, \bar{\mathbf{a}}_{l,K}^T]^T = \mathbf{f}_t(\theta_l)$ as shown in (15) and $\mathbf{p}_{l,m} = [1, e^{j\pi\beta_{l,m}}, \dots, e^{j\pi(K-1)\beta_{l,m}}]^T$ as shown in (16), the beam generated by the frequency-dependent analog beamforming vector $\mathbf{a}_{l,m}$ can be aligned with the physical direction θ_{opt} at the subcarrier frequency f_m as

$$\theta_{\text{opt}} = \arg \max_{\theta} |\eta(\mathbf{a}_{l,m}, \theta, f_m)| = \frac{\theta_l}{\xi_m} + \frac{\beta_{l,m}}{\xi_m P}, \quad (17)$$

where $P = N_t/K$, and the normalized array gain achieved by the analog beamforming vector $\mathbf{a}_{l,m}$ in the physical direction θ_{opt} is $\eta(\mathbf{a}_{l,m}, \theta_{\text{opt}}, f_m) = \frac{K}{N_t} \Xi_P(\frac{\beta_{l,m}}{P})$.

Proof: See Appendix.

We can know from **Lemma 2** that the direction rotation factor $\beta_{l,m}$ can change the physical direction of the beam from $\theta_{l,m} = \frac{\theta_l}{\xi_m}$ achieved by the classical hybrid precoding architecture to $\theta_{\text{opt}} = \frac{\theta_l}{\xi_m} + \frac{\beta_{l,m}}{\xi_m P}$ achieved by the proposed DPP architecture. Therefore, to compensate for the array gain loss caused by the beam split effect across the entire bandwidth, we should make $\theta_{\text{opt}} = \theta_l$, i.e.,

$$\frac{\theta_l}{\xi_m} + \frac{\beta_{l,m}}{\xi_m P} = \theta_l. \quad (18)$$

Then, we can easily obtain the direction rotation factor $\beta_{l,m}$ as

$$\beta_{l,m} = (\xi_m - 1)P\theta_l. \quad (19)$$

By setting the direction rotation factor $\beta_{l,m}$ as (19), the array gain loss incurred by the beam split effect can be efficiently eliminated, since the beam generated by the analog beamforming vector $\mathbf{a}_{l,m}$ is aligned with the physical direction θ_l across the entire bandwidth for any subcarrier frequency f_m . It should be noted that as we can see from the Appendix, the beamwidths of beams generated by $\mathbf{a}_{l,m}$ is approximately decided by $|\Xi_K(P(\theta_l - \xi_m\theta) + \beta_{l,m})|$, which is equal to the original beam generated by $\mathbf{a}_l = \mathbf{f}_t(\theta_l)$ as $\frac{4}{N_t}$.

An important problem in the proposed DPP is that how many TD elements are sufficient to mitigate the beam split at all subcarriers in all possible physical directions. Note that the value of the direction rotation factor is restricted by $\beta_{l,m} \in [-1, 1]$. Thus, the direction rotation factor $\beta_{l,m}$ calculated as (19) should lie in $[-1, 1]$ in all possible physical directions at all subcarrier frequencies f_m . This means

$$-1 \leq (\xi_m - 1)P\theta_l \leq 1. \quad (20)$$

Recalling that $\theta_l \in [-1, 1]$ and $\frac{f_1}{f_c} \leq \xi_m \leq \frac{f_M}{f_c}$, we have

$$P \leq \frac{1}{\frac{f_M}{f_c} - 1}. \quad (21)$$

Substituting $K = N_t/P$ into (21), we can obtain the constraint on the number of the TD elements K to compensate for the array gain caused by the beam split effect at all subcarriers in all possible physical directions, which should be

$$K \geq \left(\frac{f_M}{f_c} - 1\right)N_t. \quad (22)$$

From (22), we can observe that the number of TD elements K increases linearly with the ratio between the maximum subcarrier frequency f_M and the central frequency f_c . Since f_M/f_c is proportional to the bandwidth B , we can conclude that the number of TD elements K increases linearly with the bandwidth B . This means that when the bandwidth is narrow, a small number of TD elements K is enough to compensate for the array gain loss. While, the number of TD elements should be accordingly increased with the serious beam split effect. Specifically, in narrowband system with the assumption $f_m \approx f_c$, the number of TD elements K becomes 0 according to (22). This means that the proposed DPP architecture degenerates into the classical hybrid precoding architecture in the narrowband case, which indicates that the classical hybrid precoding architecture is a special case of the proposed DPP architecture.

D. Array gain performance of DPP

In this subsection, we will provide the theoretical analysis of the array gain achieved by the proposed DPP architecture. By adapting the constraint of K in (22), the array gain performance achieved by the proposed DPP can be derived. From (57), for the m -th subcarrier, we have

$$\eta(\mathbf{a}_{l,m}, \theta_l, f_m) = \frac{K}{N_t} \left| \Xi_P\left(\frac{\beta_{l,m}}{P}\right) \right|, \quad (23)$$

where the θ_{opt} is replaced by θ_l , because we have $\theta_{\text{opt}} = \theta_l$ by the proposed DPP. By substituting $\beta_{l,m} = (\xi_m - 1)P\theta_l$ in (19) into (23), the expectation of the array gain achieved by the beamforming vector $\mathbf{a}_{l,m}$ at all subcarriers $m = 1, 2, \dots, M$ in all possible physical direction $\theta_{l,c} \in [-1, 1]$ can be denoted as

$$\mathbb{E}(\eta(\mathbf{a}_{l,m}, \theta_l, f_m)) = \frac{K}{2MN_t} \sum_{m=1}^M \int_{-1}^1 |\Xi_P((\xi_m - 1)\theta_l)| d\theta_l. \quad (24)$$

Since it is difficult to calculate the integration of the Dirichlet sinc function, we utilize a polynomial to fit it by three points $(-1, |\Xi_P(1 - \xi_m)|)$, $(0, P)$ and $(1, |\Xi_P(\xi_m - 1)|)$. Then, we have

$$\begin{aligned} \int_{-1}^1 |\Xi_P((\xi_m - 1)\theta_l)| d\theta_l &\approx \int_{-1}^1 [(\Xi_P(\xi_m - 1) - P)\theta_l^2 + P] d\theta_l \\ &= \frac{2}{3}|\Xi_P(\xi_m - 1)| + \frac{4}{3}P. \end{aligned} \quad (25)$$

By substituting (25) into (24), we have

$$\mathbb{E}(\eta(\mathbf{a}_{l,m}, \theta_l, f_m)) \approx \frac{K}{MN_t} \sum_{m=1}^M \left(\frac{1}{3}|\Xi_P(\xi_m - 1)| + \frac{2}{3}P \right). \quad (26)$$

It is clear from (26) that the expectation of the array gain achieved by the proposed DPP over all subcarriers in all possible physical directions is mainly decided by the normalized frequency ξ_m . Considering the constraint of (22), $\xi_m - 1$ always locates in the mainlobe of the Dirichlet sinc function Ξ_P . This guarantees the array gain achieved by the DPP is larger than $\frac{2KP}{3N_t} = 0.667$, which is much higher than the array gain achieved by the classical hybrid precoding architecture as shown in Fig. 5. For instance, when $f_c = 300$ GHz, $B = 15$ GHz, $M = 128$, $K = 8$ and $N_t = 256$, we have $\mathbb{E}(|\eta(\mathbf{a}_{l,m}, \theta_l, f_m)|) \approx 0.96$, which means the proposed DPP is able to approach the near-optimal array gain at all subcarriers in all possible physical directions.

IV. HARDWARE IMPLEMENTATION OF THE DPP

In the previous section, we have proposed the DPP architecture, where a new TD network is introduced between the RF chains and the PS network in the classical hybrid precoding architecture to provide the near-optimal array gain over the whole wide bandwidth. Moreover, through theoretical analysis, we have shown that the proposed DPP can eliminate the array gain loss caused by the beam split effect and achieve the near-optimal array gain performance. The hardware implementation of the DPP architecture is important to make the DPP concept practical in real THz massive MIMO systems. In this section, we will propose a practical hardware structure and the corresponding precoding algorithm to realize the concept of the DPP based on true-time-delayers (TTDs). Furthermore, the theoretical analysis of achievable rate is provided, which illustrates the proposed TTD based DPP (TTD-DPP) structure can realize the near-optimal achievable rate performance.

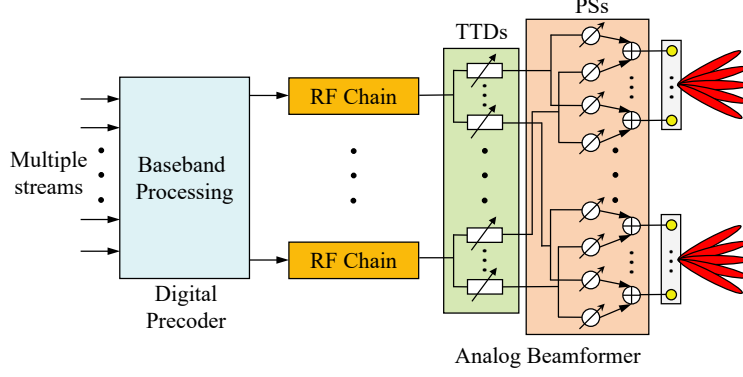


Fig. 7. The proposed TTD-DPP structure.

A. True-time-delays based DPP

Based on the intuitive idea that utilizing TTDs can be directly used to realize the TD network in the proposed DPP architecture, we propose a hardware structure called TTD-DPP, as shown in Fig. 7. In the TTD-DPP structure, each RF chain is connected to K TTDs, and each TTD is connected to $P = \frac{N_t}{K}$ PSs. The TTDs can realize the phase shift $-2\pi f_m t$ by the time delay t at frequency f_m . Therefore, the received signal y_m at the m -th subcarrier in (1) can be denoted as

$$\mathbf{y}_m = \sqrt{\rho} \mathbf{H}_m^H \mathbf{A}_u \mathbf{A}_m^{\text{TTD}} \mathbf{D}_m \mathbf{s}_m + \mathbf{n}_m, \quad (27)$$

where $\mathbf{A}_u \in \mathcal{C}^{N_t \times KN_{\text{RF}}}$ denotes the analog beamformer provided by the frequency-independent PSs with the form as

$$\mathbf{A}_u = [\mathbf{A}_{u,1}, \mathbf{A}_{u,2}, \dots, \mathbf{A}_{u,N_{\text{RF}}}], \quad (28)$$

where $\mathbf{A}_{u,l} = \text{blkdiag}([\bar{\mathbf{a}}_{l,1}, \bar{\mathbf{a}}_{l,1}, \dots, \bar{\mathbf{a}}_{l,K}])$ denotes the analog beamformer realized by the PSs connected to the l -th RF chain through TTDs, and $\mathbf{A}_m^{\text{TTD}} \in \mathcal{C}^{KN_{\text{RF}} \times N_{\text{RF}}}$ denotes the frequency-dependent phase shifts realized by TTDs, which satisfies

$$\mathbf{A}_m^{\text{TTD}} = \text{blkdiag}\left([e^{-j2\pi f_m t_1}, e^{-j2\pi f_m t_2}, \dots, e^{-j2\pi f_m t_{N_{\text{RF}}}}]\right), \quad (29)$$

where $\mathbf{t}_l \in \mathcal{C}^{K \times 1} = [t_{l,1}, t_{l,2}, \dots, t_{l,K}]^T$ denotes the time delays realized by K TTDs for the l -th path component.

Based on the notation above, the beamforming vector for the l -th path component $\mathbf{a}_{l,m} = [\mathbf{A}_u \mathbf{A}_m^{\text{TTD}}]_{[l,:]} = \mathbf{A}_{u,l} e^{-j2\pi f_m \mathbf{t}_l} = \text{diag}([\bar{\mathbf{a}}_{l,1}, \bar{\mathbf{a}}_{l,1}, \dots, \bar{\mathbf{a}}_{l,K}]) e^{-j2\pi f_m \mathbf{t}_l}$. Recalling (14), (15), (16), and **Lemma 2** in subsection III-C, to compensate for the beam split effect for the l -th path

component, the phase shifts provided by PSs and the time delays realized by K TTDs should satisfy

$$[\bar{\mathbf{a}}_{l,1}^T, \bar{\mathbf{a}}_{l,2}^T, \dots, \bar{\mathbf{a}}_{l,K}^T]^T = \mathbf{f}_t(\theta_l), \quad (30)$$

$$e^{-j2\pi f_m \mathbf{t}_l} = [1, e^{-j\pi\beta_{l,m}}, e^{-j\pi 2\beta_{l,m}}, \dots, e^{-j\pi(K-1)\beta_{l,m}}]^T, \quad (31)$$

where the direction rotation factor is $\beta_{l,m} = (\xi_m - 1)P\theta_l$ according to (19). Therefore, noting that the value difference between phase shifts of adjacent TTDs is equal, the time delay vector \mathbf{t}_l should be set as

$$\mathbf{t}_l = [0, s_l T_c, 2s_l T_c, \dots, (K-1)s_l T_c]^T, \quad (32)$$

where T_c is the period of the carrier frequency f_c , and s_l denotes the number of periods that should be delayed for the l -th path component. Thus, s_l should satisfy

$$-2\pi f_m s_l T_c = -\pi\beta_{l,m}. \quad (33)$$

Then, substituting $T_c = \frac{1}{f_c}$, $\xi_m = \frac{f_m}{f_c}$ and $\beta_{l,m} = (\xi_m - 1)P\theta_l$ in (19) into (33), we have

$$s_l = \frac{(\xi_m - 1)P\theta_l}{2\xi_m}. \quad (34)$$

Note that in (34), the number of periods s_l is not only decided by the fixed P and the target physical direction θ_l , but also decided by the variable relative frequency ξ_m . This makes (34) hard to realize for all M subcarriers, since s_l must be fixed due to the hardware constraint of TTDs. To solve this problem, we divide the phase shift $-\pi\beta_{l,m} = -\pi(\xi_m - 1)P\theta_l$ into two parts $-\pi\xi_m P\theta_l$ and $\pi P\theta_l$. The first part is frequency-dependent and can be realized by TTDs by setting s_l as

$$s_l = \frac{P\theta_l}{2}. \quad (35)$$

Then, the second part $\pi P\theta_l$ is frequency-independent, which can be realized by PSs by adding an extra phase shift. Specifically, the phase shifts provided by PSs $\bar{\mathbf{a}}_{l,k}$, $k = 1, 2, \dots, K$ should be changed from (30) to

$$[\bar{\mathbf{a}}_{l,1}^T, \bar{\mathbf{a}}_{l,2}^T, \dots, \bar{\mathbf{a}}_{l,K}^T]^T = [\mathbf{f}_t(\theta_l)_{[1:P]}, e^{j\pi P\theta_l} \mathbf{f}_t(\theta_l)_{[P+1:2P]}, \dots, e^{j\pi(K-1)P\theta_l} \mathbf{f}_t(\theta_l)_{[(K-1)P+1:N_t]}]. \quad (36)$$

Considering the time delays $t_{l,i}$ should be larger than 0, a small modification is required to be

operated on (35). Finally, the time delay of the i -th delayer $t_{l,i}$ should be

$$t_{l,i} = \begin{cases} (K-1) \left| \frac{P\theta_l}{2} \right| T_c + i \frac{P\theta_l}{2} T_c, & \theta_l < 0, \\ i \frac{P\theta_l}{2} T_c, & \theta_l \geq 0, \end{cases} \quad (37)$$

We can observe from (37) that the value range of $t_{l,i}$ is $t_{l,i} \in [0, \frac{N_t}{2} T_c]$ with $\theta_l \in [-1, 1]$ and $1 \leq i \leq K$. For example, when the central frequency f_c is 300 GHz, the number of antennas N_t is 256, and the number of TTDs K is $K = 16$, the range of time delays provided by the TTDs is between 0 and 426 ps. It should be noted that this range of time delays can be realized by many existing efficient TTDs [26]–[29], e.g., the TTD designed based on inductance-capacitance artificial transmission lines in [29] can realize a maximum time delay of 508 ps with a 4 ps time delay step, and it can support 20 GHz bandwidth, which are able to support the practical hardware implementation of the TTD-DPP.

Algorithm 1 Hybrid precoding for TTD-DPP.

Inputs:

Channel \mathbf{H}_m ; Physical direction θ_l

Output:

Hybrid precoder \mathbf{A}_u , $\mathbf{A}_m^{\text{TTD}}$, and \mathbf{D}_m

- 1: **for** $l \in \{1, 2, \dots, N_{\text{RF}}\}$ **do**
 - 2: $[\bar{\mathbf{a}}_{l,1}^T, \dots, \bar{\mathbf{a}}_{l,K}^T]^T = [\mathbf{f}_t(\theta_l)_{[1:P]}, e^{j\pi P\theta_l} \mathbf{f}_t(\theta_l)_{[P+1:2P]}, \dots, e^{j\pi(K-1)P\theta_l} \mathbf{f}_t(\theta_l)_{[(K-1)P+1:N_t]}]$
 - 3: $\mathbf{A}_{u,l} = \text{blkdiag}([\bar{\mathbf{a}}_{l,1}, \bar{\mathbf{a}}_{l,1}, \dots, \bar{\mathbf{a}}_{l,K}])$
 - 4: $\mathbf{A}_u = [\mathbf{A}_{u,1}, \mathbf{A}_{u,2}, \dots, \mathbf{A}_{u,N_{\text{RF}}}]$
 - 5: $s_l = P\theta_l/2$
 - 6: $t_{l,i} = \begin{cases} (K-1) \left| \frac{P\theta_l}{2} \right| T_c + i \frac{P\theta_l}{2} T_c, & \theta_l < 0, \\ i \frac{P\theta_l}{2} T_c, & \theta_l \geq 0, \end{cases}$
 - 7: $\mathbf{t}_l = [t_{l,1}, t_{l,2}, \dots, t_{l,K}]$
 - 8: **end for**
 - 9: $\mathbf{A}_u = [\mathbf{A}_{u,1}, \mathbf{A}_{u,2}, \dots, \mathbf{A}_{u,N_{\text{RF}}}]$
 - 10: **for** $m \in \{1, 2, \dots, M\}$ **do**
 - 11: $\mathbf{A}_m^{\text{TTD}} = \text{blkdiag}\left([e^{-j2\pi f_m \mathbf{t}_1}, \dots, e^{-j2\pi f_m \mathbf{t}_{N_{\text{RF}}}}]\right)$
 - 12: $\mathbf{H}_{m,\text{eq}} = \mathbf{H}_m^H \mathbf{A}_u \mathbf{A}_m^{\text{TTD}}$
 - 13: $\mathbf{D}_m = \mu \mathbf{V}_{m,\text{eq},[1:N_{\text{RF}}]}, \mathbf{H}_{m,\text{eq}} = \mathbf{U}_{m,\text{eq}} \mathbf{\Sigma}_{m,\text{eq}} \mathbf{V}_{m,\text{eq}}^H$
 - 14: **end for**
 - 15: **return** \mathbf{A}_u , $\mathbf{A}_m^{\text{TTD}}$ and \mathbf{D}_m
-

By setting $\bar{\mathbf{a}}_{l,i}$ and $t_{l,i}$ for $i = 1, 2, \dots, K$ as (36) and (37), the TTD-DPP structure can compensate for the array gain loss caused by the beam split effect for the l -th path component. Based on the derivation above, we propose a hybrid precoding algorithm for the TTD-DPP structure, where the key idea is to generate beams towards different physical directions of path components at first, and then the time delays are calculated accordingly to make the beam aligned with the physical direction at each subcarrier. Specifically, the pseudo-code is shown in **Algorithm 1**. At first, for each path component, the analog beamformer $\mathbf{A}_{u,l}$ is calculated in steps 2-4. Then, the time delays that should be delayed by K TTDs are generated in steps 5-7. After that, for each subcarrier frequency, the analog beamformer $\mathbf{A}_m^{\text{TTD}}$ is generated in step 11. Finally, the digital precoder \mathbf{D}_m is also calculated based on singular value decomposition (SVD) precoding in steps 12 and 13, where μ is the power normalization coefficient.

In the TTD-DPP structure, $K \times N_{\text{RF}}$ TTDs are used based on the classical hybrid precoding structure. Although the power consumption of a TTD is much higher than a PS, the increased power consumption of TTD-DPP compared with the classical hybrid precoding structure is limited since $K \times N_{\text{RF}} \ll N_t$. This will also be verified in simulation results that a small number of TTDs is able to compensate for the beam split effect across the entire bandwidth.

In addition, it should be emphasized that we only provide one practical hardware implementation of DPP in this paper. Actually, any hardware component that can realize frequency-dependent phase shifts is able to realize the concept of DPP as shown in Subsection III-C. For instance, multiple RF chains can be used to realize frequency-dependent phase shifts in the baseband. Specifically, N_{RF} RF chain group with each group containing K RF chains can be utilized, where each RF chain group connects to all antenna elements through PSs in a sub-connected manner. In this way, when the PSs generate frequency-independent beams according to (15) and the baseband signal processing realize the frequency-dependent phase shifts β_m according to (19), the mechanism of the DPP proved in **Lemma 2** can also be realized, and thus the beam split effect can be eliminated. In the next subsection, the achievable rate performance of the TTD-DPP will be provided through theoretical analysis.

B. Achievable rate performance

In this subsection, we will derive the achievable rate of the proposed TTD-DPP structure. For the wideband THz massive MIMO systems with M subcarriers, the achievable rate R can be

presented as [21]

$$R = \sum_{m=1}^M R_m = \sum_{m=1}^M \log_2 \left(\left| \mathbf{I}_{N_r} + \frac{\rho}{N_s \sigma^2} \mathbf{H}_m \mathbf{A}_m \mathbf{D}_m \mathbf{D}_m^H \mathbf{A}_m^H \mathbf{H}_m^H \right| \right), \quad (38)$$

where R_m denotes the achievable rate at the m -th subcarrier, and $\mathbf{A}_m = \mathbf{A}_u \mathbf{A}_m^{\text{TTD}}$ for the TTD-DPP. By utilizing the ordered SVD of \mathbf{H}_m as $\mathbf{H}_m = \mathbf{U}_m \Sigma_m^f \mathbf{V}_m^H$, the achievable rate R_m can be converted into [15]

$$R_m = \log_2 \left(\left| \mathbf{I}_{d_m} + \frac{\rho}{N_s \sigma^2} \Sigma_m^{f^2} \mathbf{V}_m^H \mathbf{A}_m \mathbf{D}_m \mathbf{D}_m^H \mathbf{A}_m^H \mathbf{V}_m^f \right| \right), \quad (39)$$

where the diagonal matrix $\Sigma_m^f = \text{diag}([\lambda_1, \lambda_2, \dots, \lambda_{d_m}]) \in \mathcal{C}^{d_m \times d_m}$ ($\lambda_i, i = 1, 2, \dots, d_m$) representing the singular value of \mathbf{H}_m , and the matrix $\mathbf{V}_m^f \in \mathcal{C}^{N_t \times d_m}$ with $\mathbf{V}_m^H \mathbf{V}_m^f = \mathbf{I}_{d_m}$ are obtained from the ordered SVD of the channel \mathbf{H}_m , where d_m denotes the rank of \mathbf{H}_m .

Without loss of generality, we assume that the parameters (N_t, N_{RF}, N_s) for DPP are delicately designed so that the multiplexing gain from the multi-path channel can be fully exploited. This assumption can be easily satisfied in practical THz massive MIMO systems [15]. Under this assumption, according to [15], (39) can be rewritten as

$$R_m = \log_2 \left(\left| \mathbf{I}_{N_s} + \frac{\rho}{N_s \sigma^2} \Sigma_m^2 \mathbf{V}_m^H \mathbf{A}_m \mathbf{D}_m \mathbf{D}_m^H \mathbf{A}_m^H \mathbf{V}_m \right| \right), \quad (40)$$

where $\Sigma_m = \Sigma_{m, [1:N_s, 1:N_s]}^f$ and $\mathbf{V}_m = \mathbf{V}_{m, [1:N_s]}^f$. Note that \mathbf{V}_m is the optimal precoding matrix without any hardware constraint. Considering the fact that the steering vectors $\mathbf{f}_t(\bar{\theta}_{l,m})$ in the channel model (3) are approximately orthogonal due to the large number of antennas [30], these vectors $\mathbf{f}_t(\bar{\theta}_{l,m})$ can form a set of orthogonal basis of $\mathbf{H}\mathbf{H}^H$. Since the columns of \mathbf{V}_m^f are also a set of orthogonal basis for $\mathbf{H}\mathbf{H}^H$, the columns of \mathbf{V}_m can be approximately seen as the linear combination of $\mathbf{f}_t(\bar{\theta}_{l,m})$ as

$$\mathbf{V}_m \approx \mathbf{A}_t \mathbf{D}_{m,\text{opt}}, \quad (41)$$

where $\mathbf{A}_t = [\mathbf{f}_t(\bar{\theta}_{1,m}), \mathbf{f}_t(\bar{\theta}_{2,m}), \dots, \mathbf{f}_t(\bar{\theta}_{N_{\text{RF}},m})]$ with $\bar{\theta}_{l,m}$ being sorted by path gains $|g_1| > |g_2| > \dots > |g_{N_{\text{RF}}}|$, and $\mathbf{D}_{m,\text{opt}} \in \mathcal{C}^{N_{\text{RF}} \times N_s}$. Note that in (41), \mathbf{V}_m and \mathbf{A}_t satisfy $\mathbf{V}_m^H \mathbf{V}_m = \mathbf{I}_{N_s}$ and $\mathbf{A}_t^H \mathbf{A}_t = \mathbf{I}_{N_{\text{RF}}}$. Therefore, the optimal digital precoder $\mathbf{D}_{m,\text{opt}}$ also satisfies $\mathbf{D}_{m,\text{opt}}^H \mathbf{D}_{m,\text{opt}} = \mathbf{I}_{N_s}$. Obviously, when $\mathbf{A}_m = \mathbf{A}_t$ and $\mathbf{D}_m = \mathbf{D}_{m,\text{opt}}$, the optimal achievable rate $R_{m,\text{opt}}$ can be derived

as

$$R_{m,\text{opt}} = \log_2 \left(\left| \mathbf{I}_{N_s} + \frac{\rho}{N_s \sigma^2} \boldsymbol{\Sigma}_m^2 \right| \right). \quad (42)$$

However, for the proposed TTD-DPP, the near-optimal precoder $\mathbf{A}_m = \mathbf{A}_t$ and $\mathbf{D}_m = \mathbf{D}_{m,\text{opt}}$ cannot be achieved at all subcarriers, since the analog beamforming vectors $\mathbf{a}_{l,m}$ as shown in (14) in DPP cannot be equal to $\mathbf{f}_t(\bar{\theta}_{l,m})$ at all subcarriers. Specifically, we can obtain the achievable rate $R_{m,\text{TTD}}$ of the proposed TTD-DPP by substituting (41) into (40) as

$$R_{m,\text{TTD}} = \log_2 \left(\left| \mathbf{I}_{N_s} + \frac{\rho}{N_s \sigma^2} \boldsymbol{\Sigma}_m^2 \mathbf{V}_{m,\text{eq}}^H \mathbf{V}_{m,\text{eq}} \right| \right), \quad (43)$$

where $R_{m,\text{TTD}}$ is the achievable rate achieved by the TTD-DPP, and $\mathbf{V}_{m,\text{eq}} = \mathbf{D}_m^H \mathbf{A}_m^H \mathbf{A}_t \mathbf{D}_{m,\text{opt}}$. Considering that the columns of \mathbf{A}_m are the analog beamforming vectors generated by the DPP, which can generate beams aligned with the physical direction θ_l , and the steering vectors towards different physical directions are approximately orthogonal [30], we have

$$\mathbf{A}_m^H \mathbf{A}_t = \text{blkdiag}([\mathbf{a}_{1,m}^H \mathbf{f}_t(\bar{\theta}_{1,m}), \mathbf{a}_{2,m}^H \mathbf{f}_t(\bar{\theta}_{2,m}), \dots, \mathbf{a}_{N_{\text{RF}},m}^H \mathbf{f}_t(\bar{\theta}_{N_{\text{RF}},m})]), \quad (44)$$

where $\mathbf{A}_m^H \mathbf{A}_t$ is a diagonal matrix. Recalling the definition of the array gain $\eta(\mathbf{a}_{l,m}, \theta_l, f_m) = |\mathbf{f}_t(2d \frac{f_m}{c} \theta_l)^H \mathbf{a}_{l,m}|$ and (5), we know that $\Phi_m = \mathbf{A}_m^H \mathbf{A}_t$ satisfies

$$\Phi_m^H \Phi_m = \text{blkdiag}([\eta(\mathbf{a}_{1,m}, \theta_1, f_m)^2, \eta(\mathbf{a}_{2,m}, \theta_2, f_m)^2, \dots, \eta(\mathbf{a}_{N_{\text{RF}},m}, \theta_{N_{\text{RF}}}, f_m)^2]). \quad (45)$$

Therefore, based on (45), the achievable rate $R_{m,\text{TTD}}$ becomes

$$\begin{aligned} R_{m,\text{TTD}} &= \log_2 \left(\left| \mathbf{I}_{N_s} + \frac{\rho \boldsymbol{\Sigma}_m^2 \mathbf{D}_{m,\text{opt}}^H \Phi_m^H \mathbf{D}_m \mathbf{D}_m^H \Phi_m \mathbf{D}_{m,\text{opt}}}{N_s \sigma^2} \right| \right) \\ &\stackrel{(a)}{=} \log_2 \left(\left| \mathbf{I}_{N_s} + \frac{\rho \boldsymbol{\Sigma}_m^2 \mathbf{D}_{m,\text{opt}}^H \Phi_m^H \Phi_m \mathbf{D}_{m,\text{opt}}}{N_s \sigma^2} \right| \right) \\ &\stackrel{(b)}{\approx} \log_2 \left(\left| \mathbf{I}_{N_s} + \frac{\rho \mathbb{E}(\eta(\mathbf{a}_{l,m}, \theta_l, f_m)^2) \boldsymbol{\Sigma}_m^2 \mathbf{D}_{m,\text{opt}}^H \mathbf{D}_{m,\text{opt}}}{N_s \sigma^2} \right| \right) \\ &\stackrel{(c)}{=} \log_2 \left(\left| \mathbf{I}_{N_s} + \frac{\rho}{N_s \sigma^2} \mathbb{E}(\eta(\mathbf{a}_{l,m}, \theta_l, f_m)^2) \boldsymbol{\Sigma}_m^2 \right| \right), \end{aligned} \quad (46)$$

where (a) is achieved by setting $\mathbf{D}_m = \mathbf{D}_{m,\text{opt}}$ and $\mathbf{D}_{m,\text{opt}}^H \mathbf{D}_{m,\text{opt}} = \mathbf{I}_{N_s}$, (b) comes from (45) and the assumption $\eta(\mathbf{a}_{1,m}, \theta_1, f_m)^2 \approx \eta(\mathbf{a}_{2,m}, \theta_2, f_m)^2 \approx \dots \approx \eta(\mathbf{a}_{N_{\text{RF}},m}, \theta_{N_{\text{RF}}}, f_m)^2 \approx \mathbb{E}(\eta(\mathbf{a}_{l,m}, \theta_l, f_m)^2)$ which is reasonable since the beams generated by the DPP can achieve near-

optimal array gain across the entire bandwidth as will be verified by simulation results in Section V, and (c) comes from $\mathbf{D}_{m,\text{opt}}^H \mathbf{D}_{m,\text{opt}} = \mathbf{I}_{N_s}$.

We can observe from (46) that the achievable rate $R_{m,\text{TTD}}$ is mainly decided by the array gain obtained in different physical directions at different subcarriers. This indicates that the array gain loss caused by the beam split effect is vital to the achievable rate in wideband THz massive MIMO systems. Based on (46) and (50), the ratio between the achievable rate achieved by the TTD-DPP and the optimal achievable rate can be denoted as

$$\begin{aligned} \frac{R_{m,\text{TTD}}}{R_{m,\text{opt}}} &= \frac{\log_2 \left(\left| \mathbf{I}_{N_s} + \frac{\rho}{N_s \sigma^2} \mathbb{E}(\eta(\mathbf{a}_{l,m}, \theta_l, f_m))^2 \boldsymbol{\Sigma}_m^2 \right| \right)}{\log_2 \left(\left| \mathbf{I}_{N_s} + \frac{\rho}{N_s \sigma^2} \boldsymbol{\Sigma}_m^2 \right| \right)} \\ &= \frac{\sum_{l=1}^{N_s} \log_2 \left(1 + \frac{\rho}{N_s \sigma^2} \mathbb{E}(\eta(\mathbf{a}_{l,m}, \theta_l, f_m)^2) \lambda_l^2 \right)}{\sum_{l=1}^{N_s} \log_2 \left(1 + \frac{\rho}{N_s \sigma^2} \lambda_l^2 \right)} \stackrel{(a)}{>} \frac{\sum_{l=1}^{N_s} \frac{\rho}{N_s \sigma^2} \mathbb{E}(\eta(\mathbf{a}_{l,m}, \theta_l, f_m)^2) \lambda_l^2}{\sum_{l=1}^{N_s} \frac{\rho}{N_s \sigma^2} \lambda_l^2}, \end{aligned} \quad (47)$$

where the derivation (a) is based on $\log_2(1+x) < x$ and $\eta(\mathbf{a}_{l,m}, \theta_l, f_m)^2 \leq 1$. According to (47), the ratio $R_{m,\text{TTD}}/R_{m,\text{opt}}$ can be denoted as

$$\frac{R_{m,\text{TTD}}}{R_{m,\text{opt}}} > \frac{\sum_{l=1}^{N_{\text{RF}}} \frac{\rho}{N_s \sigma^2} \mathbb{E}(\eta(\mathbf{a}_{l,m}, \theta_l, f_m)^2) \lambda_l^2}{\sum_{l=1}^{N_{\text{RF}}} \frac{\rho}{N_s \sigma^2} \lambda_l^2} = \mathbb{E} \left(\eta(\mathbf{a}_{l,m}, \theta_l, f_m)^2 \right). \quad (48)$$

In Subsection III-D, the expectation of the normalized array gain $\mathbb{E} \left(\eta(\mathbf{a}_{l,m}, \theta_l, f_m) \right)$ has been provided in (26). Similar to the process to compute $\mathbb{E} \left(\eta(\mathbf{a}_{l,m}, \theta_l, f_m) \right)$ in (25), the polynomial fitting with three points $(-1, \Xi_P(1 - \xi_m)^2)$, $(0, P^2)$ and $(1, \Xi_P(\xi_m - 1)^2)$ can be also utilized to calculate $\mathbb{E}(\eta(\mathbf{a}_{l,m}, \theta_l, f_m)^2)$ in (48) as

$$\begin{aligned} \mathbb{E} \left(\eta(\mathbf{a}_{l,m}, \theta_l, f_m)^2 \right) &= \frac{K^2}{2MN_t^2} \sum_{m=1}^M \int_{-1}^1 [\Xi_P((\xi_m - 1)\theta_l)]^2 d\theta_l \\ &\approx \frac{K^2}{2MN_t^2} \sum_{m=1}^M \int_{-1}^1 [(\Xi_P(\xi_m - 1)^2 - P^2)\theta_l^2 + P^2] d\theta_l \\ &= \frac{K^2}{MN_t^2} \sum_{m=1}^M \frac{1}{3} \Xi_P(\xi_m - 1)^2 + \frac{2}{3} P^2. \end{aligned} \quad (49)$$

It is clear from (49) that the achievable rate $R_{m,\text{TTD}}$ of the TTD-DPP structure will increase as K increases, since the mainlobe of $\Xi_P(x)$ become wider, which results in the fact that $|\Xi_P(\xi_m - 1)|$ is closer to 1. For example, when $f_c = 300$ GHz, $B = 15$ GHz, $M = 128$, $K = 8$ and $N_t = 256$, we have $\mathbb{E}(\eta(\mathbf{a}_{l,m}, \theta_l, f_m)^2) = 0.94$. This means that by adopting the proposed TTD-DPP, which

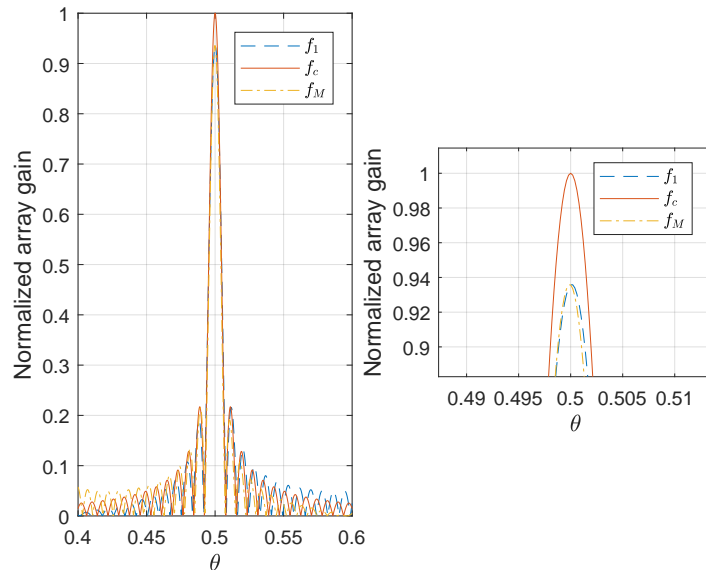


Fig. 8. Normalized array gain of beams generated by the proposed DPP structure.

is able to efficiently mitigate the beam split effect, so the near-optimal achievable rate can be achieved.

V. SIMULATION RESULTS

In this section, we provide simulation results to verify the performance of the proposed TTD-DPP to realize the concept of DPP for wideband THz massive MIMO. The main simulation

TABLE I
SYSTEM PARAMETERS FOR SIMULATIONS

The number of the BS antennas N_t	256
The number of the user antennas N_r	1, 2, 4
The number of channel paths L	4
The central frequency f_c	300 GHz
The bandwidth B	30 GHz
The number of the subcarriers M	128
The number of RF chains N_{RF}	4
The number of TD elements K	16
Physical directions of the paths $\tilde{\theta}_l, \tilde{\phi}_l$	$\mathcal{U}[-\frac{\pi}{2}, \frac{\pi}{2}]$
The transmission SNR ρ/σ^2	$-20 \sim 15$ dB

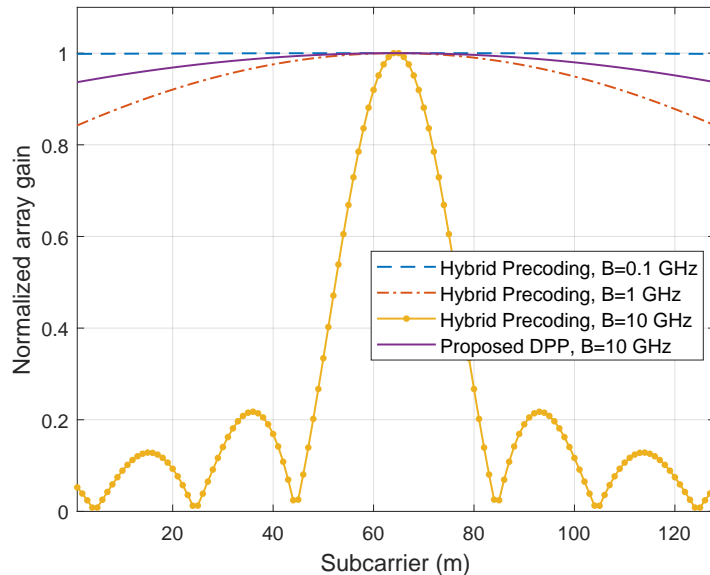


Fig. 9. Normalized array gain comparison between the classical hybrid precoding architecture and the proposed DPP architecture across the entire bandwidth (128 subcarriers).

parameters are shown in Tabel I. The ULAs are considered at the BS and the user, with $N_t = 256$ and $N_r = 1, 2, 4$. Without loss of generality, we assume that the number of streams is equal to the number of receive antennas, i.e., $N_s = N_r$. The wideband spatial channel model (3) is adopted in the simulation with $L = 4$, $f_c = 300$ GHz, $B = 30$ GHz and $M = 128$. For each path, the physical directions of the transmitter and the receiver are generated randomly as $\tilde{\theta}_l, \tilde{\phi}_l \sim \mathcal{U}[-\pi/2, \pi/2]$. The performance of classical hybrid precoding methods using PSs is also provided as the benchmark for comparison. In the proposed TTD-DPP, the number of TTDs for one RF chain is set as $K = 16$. We utilize (38) to calculate the achievable rate, in which the transmission signal-to-noise ratio (SNR) is defined as ρ/σ^2 .

Fig. 8 shows the normalized array gain against the physical direction of the beamforming vector $\mathbf{a}_{l,1}$ at the minimum subcarrier frequency f_1 , $\mathbf{a}_{l,M}$ at the maximum subcarrier frequency f_M , and the beamforming vector at the central frequency f_c , which are generated by the proposed DPP with the target physical direction $\theta_l = 0.5$. We can observe from Fig. 8 that at the subcarriers with the minimum frequency f_1 and the maximum frequency f_M , the beamforming vector $\mathbf{a}_{l,1}$ and $\mathbf{a}_{l,M}$ generated by the proposed DPP can be aligned with the target physical direction θ_l . Thus, we can conclude that by using the proposed DPP, the user can be covered by beams at different subcarrier frequencies, which efficiently mitigates the array gain loss caused by the beam split effect. For example, more than 94% of the optimal array gain can be achieved by the

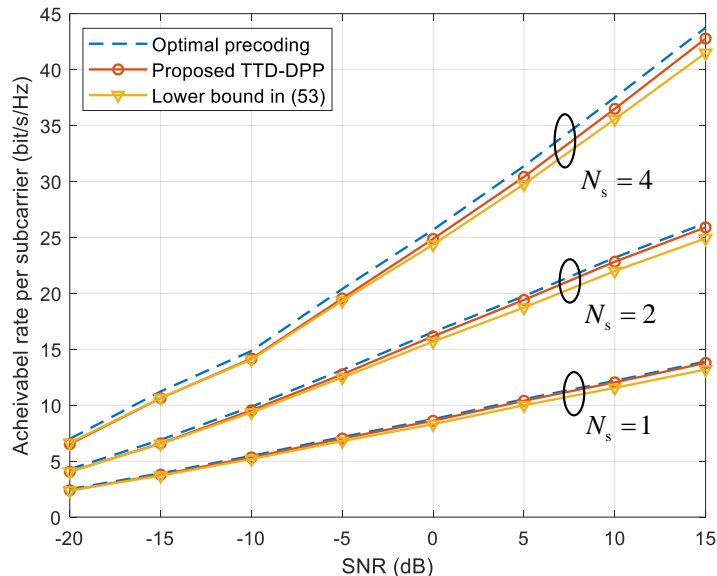


Fig. 10. Achievable rate performance versus the transmission SNR for the proposed TTD-DPP.

proposed DPP at f_1 and f_M as shown in Fig. 8.

To better illustrate the array gain achieved by the proposed DPP across the entire bandwidth, we provide the normalized array gain performance of the proposed DPP at different subcarriers in Fig. 9. The target physical direction is still set as $\theta_l = 0.5$, and the bandwidth is $B = 30$ GHz. The array gains achieved by the classical hybrid precoding structure with different bandwidths $B = 0.3, 3, 30$ GHz are also provided for comparison. We can observe from Fig. 9 that when $B = 30$ GHz, the classical hybrid precoding structure which solely controls the phase through frequency-independent PSs [15] suffers from the severe array gain loss due to the beam split effect, e.g., 80% array gain loss at most of subcarriers. On the contrary, the proposed DPP, which jointly controls the delay and phase, can realize almost flat array gain across the entire bandwidth of $B = 30$ GHz, which is much better than the classical hybrid precoding structure, and even better than the performance achieved by the classical hybrid precoding structure with a much smaller bandwidth of $B = 3$ GHz. From Fig. 8 and Fig. 9, we can conclude that for a certain target physical direction for beamforming, the proposed DPP can efficiently mitigate the array gain loss caused by the beam split effect through the joint control of delay and phase.

Fig. 10 illustrates the average achievable rate of the proposed TTD-DPP, where different numbers of data streams $N_s = 1, 2, 4$ are considered. We also provide the achievable rate performance of the optimal unconstrained fully-digital precoding [8] as the upper bound and

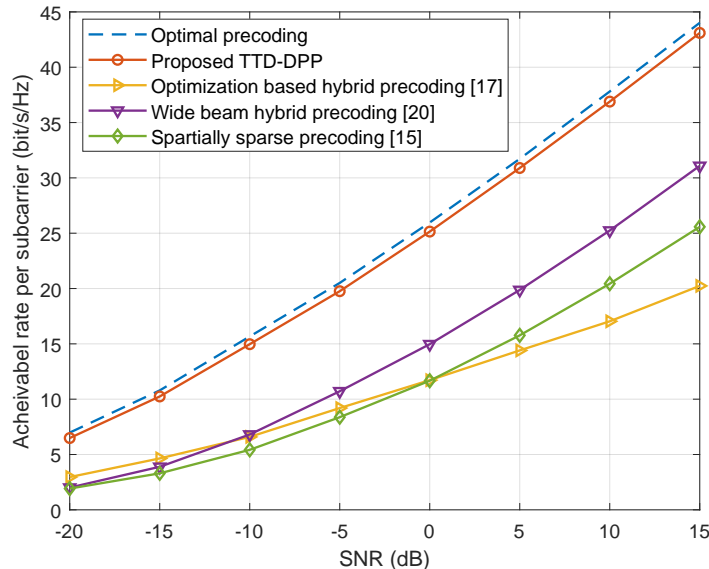


Fig. 11. Achievable rate performance comparison between the proposed scheme and existing schemes.

the theoretical result in (49) as the lower bound for comparison. We can find that the proposed TTD-DPP can achieve more than 95% of the optimal achievable rate, and the actual achievable rate is always larger than the lower bound in (49), which is consistent with the analysis in the subsection IV-B.

Fig. 11 compares the average achievable rate performance between the proposed TTD-DPP and other existing hybrid precoding schemes when $N_s = 4$. The existing solutions include the wideband hybrid precoding with the spatially sparse precoding [15], the achievable rate optimization [17], and the wide beam based hybrid precoding [20]. Specifically, we can observe from Fig. 11 that the spatially sparse precoding [15] suffer a nearly 50% achievable rate loss caused by the beam split effect. Although the achievable rate optimization [17] and wide beam based hybrid precoding [20] designed for mmWave massive MIMO systems can partially relieve the achievable rate loss incurred by the beam split effect, the performance is still unacceptable due to the very large bandwidth and antenna number in wideband THz massive MIMO systems. On the contrary, the proposed TTD-DPP scheme can significantly outperforms these existing schemes and can achieve the near-optimal achievable rate, e.g., more than 95% of the optimal achievable rate.

To better show the effect of the number of TTDs K on the proposed TTD-DPP, Fig. 12 gives the average achievable rate performance against K , where $N_s = 4$ and SNR = 10 dB are

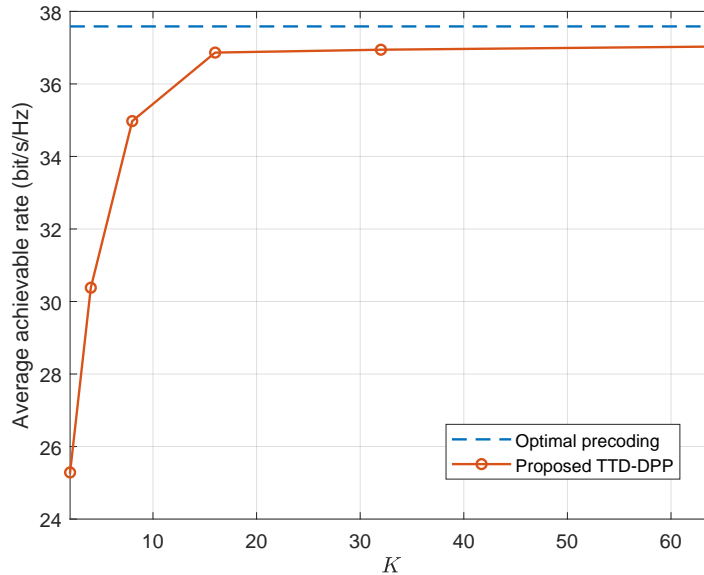


Fig. 12. Achievable rate performance versus K .

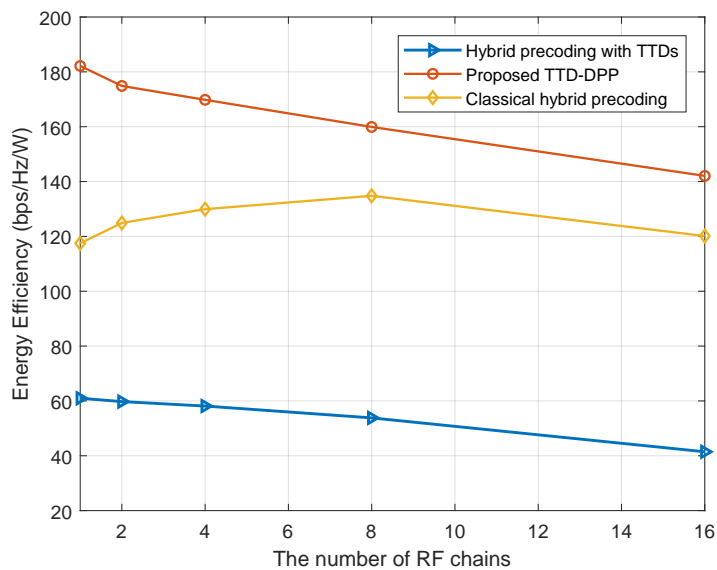


Fig. 13. Energy efficiency comparison versus the number of RF chains.

considered. From (22), we know that to compensate for the array gain loss caused by the beam split effect across the entire bandwidth, K should satisfy $K \geq 12.8$ for the parameters in TABLE I. We can observe from Fig. 12 that for the proposed TTD-DPP, the achievable rate performance increases as K becomes large, and it achieves the near-optimal achievable rate when $K \geq 16$. This trend is consistent with the theoretical result in (49).

Finally, Fig. 13 provides the energy efficiency comparison when $N_{\text{RF}} = N_s$ varies from 1

to 16. The energy efficiency is defined as the ratio between the achievable rate and the power consumption. Specifically, we compare the energy efficiency of the conventional PSs based hybrid precoding architecture [15], the TTDs based hybrid precoding where the PSs are replaced by TTDs, and the proposed TTD-DPP. The power consumption of these three schemes are denoted as P_{HP} , P_{TTD} , P_{DPP} , respectively, and we have

$$P_{\text{HP}} = P_t + P_{\text{BB}} + N_{\text{RF}}P_{\text{RF}} + N_{\text{RF}}NP_{\text{PS}}, \quad (50)$$

$$P_{\text{TTD}} = P_t + P_{\text{BB}} + N_{\text{RF}}P_{\text{RF}} + N_{\text{RF}}NP_{\text{TTD}}, \quad (51)$$

$$P_{\text{DPP}} = P_t + P_{\text{BB}} + N_{\text{RF}}P_{\text{RF}} + N_{\text{RF}}KP_{\text{TTD}} + N_{\text{RF}}NP_{\text{PS}}, \quad (52)$$

where P_t is the transmission power, and P_{BB} , P_{RF} , P_{PS} , and P_{TTD} denote the power consumption of baseband processing, RF chain, PS, and TTD, respectively. Here, we adopt the practical values as $\rho = 30$ mW [25], $P_{\text{BB}} = 300$ mW [31], $P_{\text{RF}} = 200$ mW [25], $P_{\text{PS}} = 20$ mW [31] and $P_{\text{TTD}} = 100$ mW [29]. We can observe from Fig. 13 that the proposed TTD-DPP enjoys much higher energy efficiency than the conventional hybrid precoding architecture using PSs and TTDs. Compared with the conventional hybrid precoding architecture with PSs, the proposed TTD-DPP can achieve much higher achievable rate by eliminating the achievable rate loss caused by the beam split effect, with an acceptable power consumption increase caused by the additional use of limited TTDs. Moreover, the proposed TTD-DPP also has higher energy efficiency than the conventional hybrid precoding architecture with TTDs, since much less TTDs ($N_{\text{RF}}K$ instead of $N_{\text{RF}}N$, where $K \ll N$) are utilized in the TTD-DPP. This indicates that the TDD-DPP is able to provide a better tradeoff between the achievable rate performance and power consumption, which is promising for future THz massive MIMO systems.

VI. CONCLUSIONS

In this paper, we have investigated the wideband hybrid precoding for future THz massive MIMO systems. A vital problem called beam split, i.e., the THz rainbow, where the generated beams will split into separated physical directions at different subcarrier frequencies, has been analyzed. We revealed that the beam split effect may cause serious array gain loss and achievable rate degradation in wideband THz massive MIMO systems. To solve this problem, we have proposed a DPP architecture by introducing a TD network as a new precoding layer into the conventional hybrid precoding architecture. By leveraging the TD network, the DPP architecture

can realize a delay-phase jointly controlled beamformer, which can compensate for the array gain loss caused by the beam split effect. To realize the concept of DPP, we have further proposed a hardware structure called TTD-DDP, where the frequency-dependent phase shifts provided by the TD network are realized by multiple TTDs. Theoretical analysis and simulation results have shown that the proposed DPP can eliminate the array gain loss caused by the beam split effect, so it can achieve more than 95% of the optimal array gain and achievable rate performance across the entire bandwidth in wideband THz massive MIMO systems. Potential future works may include other feasible implementations of DPP, improved algorithm to realize DPP, channel estimation [32] and beam tracking [33] for DPP, and low-cost hardware solutions such as low-resolution PSs and low-resolution ADCs/DACs [34].

APPENDIX. PROOF OF LEMMA 2

Proof: The normalized array gain achieved by the analog beamforming vector $\mathbf{a}_{l,m}$ on an arbitrary physical direction θ at the subcarrier frequency f_m can be denoted as $\eta(\mathbf{a}_{l,m}, \theta, f_m) = |\mathbf{f}_t(2d\frac{f_m}{c}\theta)^H \mathbf{a}_{l,m}|$. With $[\bar{\mathbf{a}}_{l,1}^T, \bar{\mathbf{a}}_{l,2}^T, \dots, \bar{\mathbf{a}}_{l,K}^T]^T = \mathbf{f}(\theta_l)$ and $\mathbf{p}_{l,m} = [1, e^{-j\pi\beta_{l,m}}, \dots, e^{-j\pi(K-1)\beta_{l,m}}]^T$, we have

$$\eta(\mathbf{a}_{l,m}, \theta, f_m) = \frac{1}{N_t} \left| \sum_{k=1}^K \sum_{p=1}^P e^{-j\pi[(k-1)P+(p-1)]\theta_l} e^{-j\pi(k-1)\beta_{l,m}} e^{j\pi[(k-1)P+(p-1)]\xi_m\theta} \right|. \quad (53)$$

By separating the summation on K and P , we have

$$\eta(\mathbf{a}_{l,m}, \theta, f_m) = \frac{1}{N_t} \left| \sum_{k=1}^K e^{-j\pi(k-1)[P(\theta_l - \xi_m\theta) + \beta_{l,m}]} \sum_{p=1}^P e^{-j\pi(p-1)(\theta_l - \xi_m\theta)} \right|. \quad (54)$$

Then, we can transform the summation in (54) as

$$\eta(\mathbf{a}_{l,m}, \theta, f_m) = \frac{1}{N_t} |\Xi_K(P(\theta_l - \xi_m\theta) + \beta_{l,m}) \Xi_P(\theta_l - \xi_m\theta)|. \quad (55)$$

We can see that the array gain achieved by the analog beamforming vector $\mathbf{a}_{l,m}$ is the product of two Dirichlet sinc functions, whose figures are shown in Fig. 14. Because the power of the Dirichlet sinc function is focused in the mainlobe, we can analyze the property of the array gain $\eta(\mathbf{a}_{l,m}, \theta, f_m)$ through the mainlobes of these two Dirichlet sinc functions. For the function $|\Xi_K(P(\theta_l - \xi_m\theta) + \beta_{l,m})|$ with respect to θ , the maximum value can be achieved by setting $P(\theta_l - \xi_m\theta) + \beta_{l,m} = 0$, i.e., $\theta = \theta_{K,\max} = \frac{\theta_l}{\xi_m} + \frac{\beta_{l,m}}{\xi_m P}$, and the mainlobe width of $|\Xi_K(P(\theta_{l,c} - \theta) + \beta_{l,m})|$ is $\frac{4}{N_t}$. Similarly for $|\Xi_P(\theta_{l,c} - \xi_m\theta)|$, the maximum value can be achieved

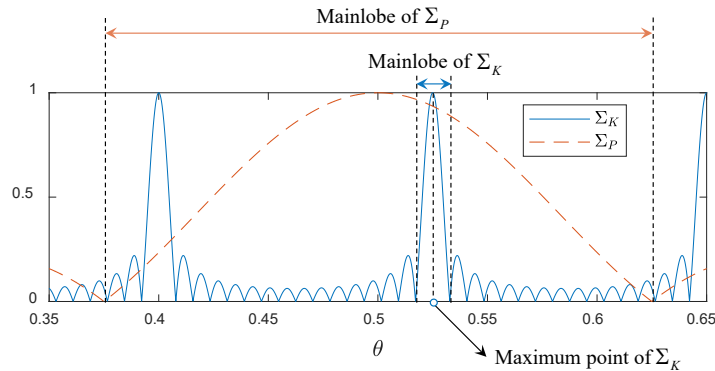


Fig. 14. The two of Dirichlet sinc functions, where Ξ_K denotes $|\frac{1}{K}\Xi_K(P(\theta_l - \xi_m\theta) + \beta_{l,m})|$ and $|\Xi_P|$ denotes $|\frac{1}{P}\Xi_P(\theta_l - \xi_m\theta)|$.

when $\theta = \theta_{P,\max} = \frac{\theta_l}{\xi_m}$ and the mainlobe width is $\frac{4}{P}$. Considering that the available value range of the direction rotation factor is $\beta_{l,m} \in [-1, 1]$, we have $\theta_{K,\max} \in [\frac{\theta_l}{\xi_m} - \frac{1}{\xi_m P}, \frac{\theta_l}{\xi_m} + \frac{1}{\xi_m P}]$, which means that $\theta_{K,\max}$ locates in the mainlobe of $|\Xi_P(\theta_l - \xi_m\theta)|$ whose range is $[\frac{\theta_l}{\xi_m} - \frac{2}{\xi_m P}, \frac{\theta_l}{\xi_m} + \frac{2}{\xi_m P}]$. In addition, considering $P = N_t/K$, the mainlobe width of $|\Xi_P(\theta_l - \xi_m\theta)|$ is $\frac{4}{P}$ which is K times wider than that of $|\Xi_K(P(\theta_l - \xi_m\theta) + \beta_{l,m})|$, whose mainlobe width is $\frac{4}{N_t}$. Therefore, we can conclude that the variation of $|\Xi_P(\theta_l - \xi_m\theta)|$ in the mainlobe of $|\Xi_K(P(\theta_l - \xi_m\theta) + \beta_{l,m})|$ is much smaller than the variation of $|\Xi_K(P(\theta_l - \xi_m\theta) + \beta_{l,m})|$, which is shown in Fig. 14. Therefore, the maximum value of the array gain $\eta(\mathbf{a}_{l,m}, \theta, f_m)$ can be approximately considered to be decided by $|\Xi_K(P(\theta_l - \xi_m\theta) + \beta_{l,m})|$. Thus, we have

$$\theta_{\text{opt}} = \arg \max_{\theta} \eta(\mathbf{a}_{l,m}, \theta, f_m) = \theta_{K,\max} = \frac{\theta_l}{\xi_m} + \frac{\beta_{l,m}}{\xi_m P}. \quad (56)$$

Then, the array gain achieved by $\mathbf{a}_{l,m}$ at this physical direction θ_{opt} can be denoted by substituting (56) into (55) as

$$|\eta(\mathbf{a}_{l,m}, \theta_{\text{opt}}, f_m)| = \frac{1}{N_t} |\Xi_K(0)\Xi_P(\theta_l - \theta_{\text{opt}})| = \left| \frac{K}{N_t} \Xi_P\left(\frac{\beta_{l,m}}{P}\right) \right|, \quad (57)$$

which completes the proof. ■

REFERENCES

- [1] J. Tan and L. Dai, "Delay-phase precoding for THz massive MIMO with beam split," in *Proc. IEEE Global Commun. Conf.*, Dec. 2019, pp. 1–6.
- [2] T. S. Rappaport, Y. Xing, O. Kanhere, S. Ju, A. Madanayake, S. Mandal, A. Alkhateeb, and G. C. Trichopoulos, "Wireless communications and applications above 100 GHz: Opportunities and challenges for 6G and beyond," *IEEE Access*, vol. 7, pp. 78 729–78 757, Jun. 2019.

- [3] A. S. Cacciapuoti, K. Sankhe, M. Caleffi, and K. R. Chowdhury, "Beyond 5G: THz-based medium access protocol for mobile heterogeneous networks," *IEEE Commun. Mag.*, vol. 56, no. 6, pp. 110–115, Jun. 2018.
- [4] Z. Chen, X. Ma, B. Zhang, Y. Zhang, Z. Niu, N. Kuang, W. Chen, L. Li, and S. Li, "A survey on Terahertz communications," *China Commun.*, vol. 16, no. 2, pp. 1–35, Feb. 2019.
- [5] I. F. Akyildiz, J. M. Jornet, and C. Han, "Teranets: ultra-broadband communication networks in the terahertz band," *IEEE Wireless Commun.*, vol. 21, no. 4, pp. 130–135, Aug. 2014.
- [6] —, "Terahertz band: Next frontier for wireless communications," *Phys. Commun.*, vol. 12, no. 2, pp. 16–32, Sep. 2014.
- [7] H. Song and T. Nagatsuma, "Present and future of Terahertz communications," *IEEE Trans. THz Sci. Technol.*, vol. 1, no. 1, pp. 256–263, Sep. 2011.
- [8] S. Mumtaz, J. Rodriguez, and L. Dai, *MmWave Massive MIMO: A Paradigm for 5G*. Academic Press, Elsevier, 2016.
- [9] B. Peng, K. Guan, and T. Kurner, "Cooperative dynamic angle of arrival estimation considering space-time correlations for Terahertz communications," *IEEE Trans. Wireless Commun.*, vol. 17, no. 9, pp. 6029–6041, Sep. 2018.
- [10] L. You, X. Gao, G. Y. Li, X. Xia, and N. Ma, "BDMA for millimeter-wave/terahertz massive MIMO transmission with per-beam synchronization," *IEEE J. Sel. Areas Commun.*, vol. 35, no. 7, pp. 1550–1563, Jul. 2017.
- [11] X. Gao, L. Dai, Y. Zhang, T. Xie, X. Dai, and Z. Wang, "Fast channel tracking for Terahertz beamspace massive MIMO systems," *IEEE Trans. Veh. Technol.*, vol. 66, no. 7, pp. 5689–5696, Jul. 2017.
- [12] J. A. Zhang, X. Huang, V. Dyadyuk, and Y. J. Guo, "Massive hybrid antenna array for millimeter-wave cellular communications," *IEEE Wireless Commun.*, vol. 22, no. 1, pp. 79–87, Feb. 2015.
- [13] X. Gao, L. Dai, and A. M. Sayeed, "Low RF-complexity technologies to enable millimeter-wave MIMO with large antenna array for 5G wireless communications," *IEEE Commun. Mag.*, vol. 56, no. 4, pp. 211–217, Apr. 2018.
- [14] C. Han and Y. Chen, "Propagation modeling for wireless communications in the terahertz band," *IEEE Commun. Mag.*, vol. 56, no. 6, pp. 96–101, Jun. 2018.
- [15] O. E. Ayach, S. Rajagopal, S. Abu-Surra, Z. Pi, and R. W. Heath, "Spatially sparse precoding in millimeter wave MIMO systems," *IEEE Trans. Wireless Commun.*, vol. 13, no. 3, pp. 1499–1513, Mar. 2014.
- [16] B. Wang, F. Gao, S. Jin, H. Lin, G. Y. Li, S. Sun, and T. S. Rappaport, "Spatial-wideband effect in massive MIMO with application in mmwave systems," *IEEE Commun. Mag.*, vol. 56, no. 12, pp. 134–141, Dec. 2018.
- [17] S. Park, A. Alkhateeb, and R. W. Heath, "Dynamic subarrays for hybrid precoding in wideband mmWave MIMO systems," *IEEE Trans. Wireless Commun.*, vol. 16, no. 5, pp. 2907–2920, May 2017.
- [18] L. Kong, S. Han, and C. Yang, "Hybrid precoding with rate and coverage constraints for wideband massive MIMO systems," *IEEE Trans. Wireless Commun.*, vol. 17, no. 7, pp. 4634–4647, Jul. 2018.
- [19] M. Cai, K. Gao, D. Nie, B. Hochwald, J. N. Laneman, H. Huang, and K. Liu, "Effect of wideband beam squint on codebook design in phased-array wireless systems," in *Proc. IEEE Global Commun. Conf.*, Dec. 2016, pp. 1–6.
- [20] X. Liu and D. Qiao, "Space-time block coding-based beamforming for beam squint compensation," *IEEE Wireless Commun. Lett.*, vol. 8, no. 1, pp. 241–244, Feb. 2019.
- [21] D. Tse and P. Viswanath, *Fundamentals of Wireless Communication*. Cambridge, U.K.: Cambridge Univ. Press, 2005.
- [22] R. W. Heath, N. Gonzalez-Prelcic, S. Rangan, W. Roh, and A. M. Sayeed, "An overview of signal processing techniques for millimeter wave MIMO systems," *IEEE J. Sel. Top. Signal Process.*, vol. 10, no. 3, pp. 436–453, Apr. 2016.
- [23] A. M. Sayeed, "Deconstructing multiantenna fading channels," *IEEE Trans Signal Process.*, vol. 50, no. 10, pp. 2563–2579, Oct. 2002.
- [24] H. Hashemi, T. Chu, and J. Roderick, "Integrated true-time-delay-based ultra-wideband array processing," *IEEE Commun. Mag.*, vol. 46, no. 9, pp. 162–172, Sep. 2008.

- [25] X. Gao, L. Dai, S. Han, C. L. I, and R. W. Heath, "Energy-efficient hybrid analog and digital precoding for mmwave MIMO systems with large antenna arrays," *IEEE J. Sel. Areas Commun.*, vol. 34, no. 4, pp. 998–1009, Apr. 2016.
- [26] P. Chen, C. Argyropoulos, and A. Alu, "Terahertz antenna phase shifters using integrally-gated graphene transmission-lines," *IEEE Trans. Antennas Propag.*, vol. 61, no. 4, pp. 1528–1537, Apr. 2013.
- [27] A. A. Ibrahim, H. N. Shaman, and K. Sarabandi, "A sub-THz rectangular waveguide phase shifter using piezoelectric-based tunable artificial magnetic conductor," *IEEE Trans. THz Sci. Technol.*, vol. 8, no. 6, pp. 666–680, Nov. 2018.
- [28] I. Mondal and N. Krishnapura, "A 2-GHz bandwidth, 0.25-1.7 ns true-time-delay element using a variable-order all-pass filter architecture in 0.13 μm CMOS," *IEEE J. Solid-State Circuits*, vol. 52, no. 8, pp. 2180–2193, Aug. 2017.
- [29] M. Cho, I. Song, and J. D. Cressler, "A true time delay-based SiGe bi-directional T/R chipset for large-scale wideband timed array antennas," in *Proc. 2018 IEEE Radio Frequency Integrated Circuits Symposium*, 2018, pp. 272–275.
- [30] W. Shen, L. Dai, B. Shim, Z. Wang, and R. W. Heath, "Channel feedback based on AoD-adaptive subspace codebook in FDD massive MIMO systems," *IEEE Trans. Commun.*, vol. 66, no. 11, pp. 5235–5248, Nov. 2018.
- [31] R. Mendez-Rial, C. Rusu, N. Gonzalez-Prelcic, A. Alkhateeb, and R. W. Heath, "Hybrid MIMO architectures for millimeter wave communications: Phase shifters or switches?" *IEEE Access*, vol. 4, pp. 247–267, Jan. 2016.
- [32] J. Choi, D. J. Love, and P. Bidigare, "Downlink training techniques for FDD massive MIMO systems: Open-loop and closed-loop training with memory," *IEEE J. Sel. Top. Signal Process.*, vol. 8, no. 5, pp. 802–814, Oct. 2014.
- [33] L. Lian, A. Liu, and V. K. N. Lau, "Exploiting dynamic sparsity for downlink FDD-massive MIMO channel tracking," *IEEE Trans. Signal Process.*, vol. 67, no. 8, pp. 2007–2021, Apr. 2019.
- [34] P. Raviteja, Y. Hong, and E. Viterbo, "Millimeter wave analog beamforming with low resolution phase shifters for multiuser uplink," *IEEE Trans. Veh. Technol.*, vol. 67, no. 4, pp. 3205–3215, Apr. 2018.